Natural and anthropogenic influence on tropospheric ozone variability over the Tropical Atlantic unveiled by satellite and in situ observations

Sachiko Okamoto[1, a], Juan Cuesta[1], Gaëlle Dufour[2], Maxim Eremenko[1], Kazuyuki Miyazaki[3], Cathy Boonne[4], Hiroshi Tanimoto[5], Jeff Peischl[6] and Chelsea Thompson[6]

[1] Univ Paris Est Créteil and Université de Paris Cité, CNRS, LISA, F-94010 Créteil, France

[2] Université de Paris Cité and Univ Paris Est Créteil, CNRS, LISA, F-75013 Paris, France

[3] Jet Propulsion Laboratory (JPL), California Institute of Technology, Pasadena, 91109 CA, USA

[4] Institut Pierre Simon Laplace (IPSL), AERIS data centre, Paris, 75252, France

[5] National Institute for Environmental Studies, Tsukuba, 350-8506, Japan

[6] NOAA Chemical Sciences Laboratory, Boulder, CO, 80305, USA

[a] now at : National Institute for Environmental Studies, Tsukuba, 350-8506, Japan

Correspondence to: Sachiko Okamoto (okamoto.sachiko@nies.go.jp) and Juan Cuesta (cuesta@lisa.ipsl.fr)

Abstract. Tropospheric ozone over the South and Tropical Atlantic plays an important role in the photochemistry and energy budget of the atmosphere. In this remote region, tropospheric ozone estimates from reanalysis datasets show the largest discrepancies. The present study characterises the vertical and horizontal distribution of tropospheric ozone over the South and Tropical Atlantic during February and October 2017 using a multispectral satellite approach called IASI+GOME2 and in situ airborne measurements from the Atmospheric Tomography Mission (ATom). These observations are compared with two global chemistry reanalysis products: the Copernicus Atmosphere Monitoring Service reanalysis and the Tropospheric Chemistry Reanalysis version 2. These datasets show air masses enriched in ozone precursors from biomass burning sources over Western and Central Africa lifted into the middle and upper troposphere by strong upward motions; and stratospheric intrusions in the descending branches of the Hadley cells over the Southern Atlantic. Air masses in the Tropics are also influenced by lightning and stratospheric downdrafts. According to in situ measurements of chemical tracers, tropospheric ozone is attributed to biomass burning emissions of ozone precursors is ~13 ppb (~17 %) over 7 km (25° S–5° N) and ~38 ppb (~50 %) over 3 km (25° S–15° S). Intercomparisons suggest significant overestimations of tropospheric ozone from the two chemistry reanalyses at the lowermost (upper) troposphere over the Atlantic north (south) of the Equator, as related to anthropogenic North American sources (Hadley descending branch), as compared to satellite and in situ observations.

1 Introduction

Tropospheric ozone is one of the key gases in the atmosphere because it is a major greenhouse gas (Szopa et al., 2021) and it plays an important role in determining the oxidising capacity of the troposphere (Monks et al., 2015). The main source of tropospheric ozone is in situ photochemical production via oxidation of non-methane volatile organic compounds (NMVOCs), carbon monoxide (CO), and methane (CH_4), in the presence of nitrogen oxides (NO_X) (e.g., Atkinson, 2000). These ozone precursors originate from both anthropogenic (fossil fuel combustion in power plants, industrial activities, transportation and crop burning) and natural sources (wetland CH_4 emissions, wildfires, biogenic hydrocarbon emissions, lightning and soil NO_X emissions) (e.g., Elshorbany et al., 2024). The abundance of tropospheric ozone is also controlled by transport from the ozone-rich stratosphere. The net influx ozone from the stratosphere was estimated at 552 ± 168 Tg, and is smaller than the amount of chemical production (5110 ± 606 Tg; Young et al., 2013). The lifetime of ozone in the troposphere ranges from a few hours in polluted urban areas to up to a few weeks in the free troposphere, but is relatively long on average (~22 days; Young et al., 2013). This allows tropospheric ozone to be transported over distances of intercontinental and hemispheric scales.

The South and Tropical Atlantic has been a region of intense interest in the ozone scientific community since Fishman and Larson (1987) identified a regional maximum in tropospheric ozone derived from satellite measurements. This discovery was the motivation for a large-scale ground and aircraft study in the southern biomass burning season in September and October 1992: IGAC/STARE/SAFARI-92/TRACE-A (International Global Atmospheric Chemistry/South Tropical Atlantic Regional Experiment/Southern African Fire Atmospheric Research Initiative/Transport and Atmospheric Chemistry near the Equator-Atlantic). SAFARI-92/TRACE-A confirmed the regional ozone feature with aircraft profiling and lidar plus ozonesondes deployed over Brazil, Ascension Island and three sites in sub-Saharan Africa. In addition, analyses of the comprehensive SAFARI-92/TRACE-A data confirmed links of the Atlantic maximum to fire activity over Africa (Fishman et al., 1996; Thompson et al., 1996) and to ozone formed from a combination of fires, deep convection and lightning activity over South America (Pickering et al., 1996). Based on ozonesonde profiles, it was estimated that the relative contributions to the Atlantic ozone were approximately two-third from African sources and one-third from South America (Thompson et al., 1996). However, dynamic influences were required for the ozone hotspot to form. Krishnamurti et al. (1996) demonstrated that recirculation within the South Atlantic gyre allowed the ozone to accumulate so that the highest ozone amounts were over the ocean rather than the continents.

Shipboard ozone sampling over the Tropical Atlantic provided additional insights into South Tropical Atlantic ozone (Thompson et al., 2000; Weller et al., 1996). These measurements suggested that the ozone maximum occurs at all seasons, not only during the peak of Southern Hemisphere burning but also when African fire activity is at its greatest north of the Inter-Tropical Convergence Zone (ITCZ). This so-called "Atlantic ozone paradox" was associated with upper tropospheric-stratospheric subsidence and lightning in addition to fires (Thompson et al., 2000). These contributions were evaluated in an early model study (Moxim and Levy, 2000). The SAFARI-92/TRACE-A experiments were instrumental in assembling the Southern Hemisphere Additional Ozonesondes (SHADOZ) network of stations that has operated from 1998 to the present day

(Thompson et al., 2017). With coordinated launches of ozonesondes from more than 10 stations across the tropics, the Atlantic maximum is a strong feature with the South Tropical Atlantic always exhibiting more tropospheric column ozone (5–15 Dobson Units, 1 DU = 2.69×10^{16} cm^{-2}). When looking at the tropospheric ozone structure across the entire tropical band, the Atlantic ozone feature leads to a zonal wave one pattern (Thompson et al., 2003).

More recently, additional studies of the role of biomass burning (van der Werf et al., 2017), biogenic sources (Sindelarova et al., 2022) and lightning (Schumann and Huntrieser, 2007) contributions to Atlantic, African and South American ozone has been conducted. Among other features, they estimate that lightning is the major driver of the dominating ozone sensitivity in the upper tropical troposphere (Nussbaumer et al., 2023; Schumann and Huntrieser, 2007). Additional analyses of tropical ozone distributions (mostly in the upper troposphere) were performed using in situ measurements onboard commercial aircrafts (Lannuque et al., 2021; Sauvage et al. 2005; 2007b; Tsivlidou et al., 2023; Yamasoe et al., 2015). This is the case of the In-Service Aircraft for a Global Observing System (IAGOS) European Research Infrastructure (e.g., Petzold et al., 2015), the former research projects the Measurement of Ozone and Water Vapour on Airbus In-service Aircraft (MOZAIC) and the Civil Aircraft for the Regular Investigation of the Atmosphere Based on an Instrument Container (CARIBIC). Their results show for example that lightning has the largest influence on the South Atlantic ozone burden (24° S–0°, 35° W–10° E), accounting for more than 37 % (Sauvage et al. 2007a). The authors quantified that the contributions of biomass burning, fossil fuel combustion, and soil NO_X emissions to the tropospheric ozone column were 6, 5, and 4 times smaller than that from lightning. In addition, the Tropical Atlantic ozone burden was more strongly influenced by NO_X from Africa than from South America. Trends in tropical tropospheric ozone have been reported using SHADOZ ozonesonde profiles (Thompson et al., 2021) and a combination of satellite, SHADOZ and IAGOS aircraft measurements (Gaudel et al., 2024). However, most of IAGOS data is acquired in the extratropical upper troposphere/lower stratosphere (UTLS) and in the tropical upper troposphere when the aircraft attain cruising altitude in the altitude band of 9–13 km (See S1 in the Supplement). Thus, the ozone regional distribution in the middle and lower troposphere over the South and Tropical Atlantic is much less documented.

Satellite observations offer a great potential to overcome the limited spatial coverage of ground-based measurements. However, standard single-band ozone retrievals are not able to provide quantitative measurements of ozone abundance within the planetary boundary layer. Ultraviolet (UV) spaceborne spectrometers, like GOME-2 (Global Ozone Monitoring Experiment-2), have been used to observe tropospheric ozone with maximum sensitivity at about 5–6 km altitude (e.g., Liu et al., 2010; Cai et al., 2012). Space-based thermal infrared (TIR) instruments, such as the Infrared Atmospheric Sounding Interferometer (IASI) on board the MetOp satellites, have shown good performance for observing ozone in the lower troposphere but with sensitivity peaking at lowest at 3 km altitude (e.g., Eremenko et al., 2008; Dufour et al., 2012). More recently, synergetic approaches using UV and TIR radiances simultaneously have been developed to improve the sensitivity to lower tropospheric ozone (e.g., Cuesta et al., 2013; Fu et al., 2018; Colombi et al., 2021). A multispectral approach called IASI+GOME2, combining IASI observations in the TIR and GOME-2 measurements in the UV, shows remarkable skills in observing the horizontal distribution of ozone concentrations in the lowermost troposphere (LMT - here after defined as the atmospheric partial column below 3 km of altitude, Cuesta et al., 2013). Air-quality-relevant capabilities of IASI+GOME2 have been

demonstrated by quantitatively describing the transport pathways, the daily evolution, and photochemical production in the lowermost troposphere during transboundary ozone pollution events across east Asia (Cuesta et al., 2018) and Europe (Cuesta et al., 2013; 2022; Okamoto et al., 2023).

By increasing computing performance and availability of satellite observations of trace gases, data assimilation has been applied with success in monitoring air quality (e.g., Flemming et al., 2015; Gelaro et al., 2017; Inness et al., 2019; Miyazaki et al., 2015; 2020). Data assimilation is a methodology that allows a physical-chemically based interpolation to fill in of the observational information gaps using a model and to provide an estimate of the most likely state and its uncertainty. Applications of data assimilation to atmospheric chemistry can improve analyses of tropospheric pollution, and can provide estimates of tropospheric emissions (Lahoz and Schneider, 2014). The result of data assimilation is termed a "reanalysis" when the data assimilation approach is performed for past data by using a consistent system. There have been several studies that compared atmospheric chemistry reanalysis products. Air pollutants including ozone and CO derived from some chemistry reanalysis products were evaluated on regional scale in East Asia (Park et al., 2020; Ryu and Min, 2021; Zhang et al., 2022) and Europe (Falk et al., 2021; Lacima et al., 2023). Huijnen et al. (2020) intercompared four atmospheric chemistry reanalysis products and reported that the standard deviation (SD) is the largest over South America, the Tropical Atlantic and Central Africa because of their differences of the representations of biomass-burning emissions and its impacts on ozone production, the representation of convective transport, and large uncertainties in biogenic emissions.

In the present paper, we intercompare ozone distributions of the multispectral satellite approach IASI+GOME2, in situ airborne measurements conducted within the Atmospheric Tomography Mission (ATom) and two tropospheric chemistry reanalysis products over the Tropical and South Atlantic in February and October 2017. Section 2 describes the satellite data, in situ observations and atmospheric chemistry reanalysis products used for the analysis. Results and discussions on the distribution of tropospheric ozone and CO over the Tropical and South Atlantic is presented in Sect. 3. Conclusions are given in the last section.

2 Data and methods

In this study, we characterize the tropospheric ozone distribution over the Tropical Atlantic using data from a satellite approach and two chemistry reanalysis products. To analyse the origin of ozone plumes, CO satellite retrievals and two chemistry reanalysis products are also employed. We consider the region covering the Atlantic Ocean between 40° S and 40° N to investigate interactions of pollution and the transport between the tropics and the subtropics.

2.1 Satellite data

2.1.1 IASI+GOME2 ozone multispectral observations

The multispectral satellite approach IASI+GOME2 is designed for observing lowermost tropospheric ozone by synergism of TIR atmospheric radiances observed by IASI and UV earth reflectances measured by GOME-2 (Cuesta et al., 2013; 2018). Both instruments are onboard the MetOp satellite series, and they both offer global coverage every day (around 09:00 local time) with a relatively fine ground resolution (12 km diameter pixels spaced by 25 km for IASI at nadir and ground pixels of 80 km × 40 km for GOME-2). Spectra and Jacobians in the IR and UV are simulated by the KOPRA (Karlsruhe Optimized and Precise Radiative transfer Algorithm; Stiller et al., 2002) and VLIDORT (Vector Linearized Discrete Ordinate Radiative Transfer; Spurr, 2006) radiative transfer codes, respectively. Ozone profiles are retrieved at the vertical grid between the surface and 60 km of altitude. The IASI+GOME2/MetOp-B ozone product including vertical profiles of ozone, averaging kernel, error estimations and quality flags is publicly available on the French data centre AERIS (https://iasi.aeris-data.fr, last access: November 2024). For reducing random errors, the product is averaged over a regular horizontal grid of 1° × 1°, in the same way as done by Cuesta et al. (2018). Ozone concentrations are provided as an average ozone volume mixing ratio in ppb within the layer, which is calculated as the ratio of each partial column of ozone and air.

2.1.2 IASI carbon monoxide retrievals

The CO retrievals used in this study are derived from IASI radiances using the FORLI algorithm (Fast Optimal Retrievals on Layers for IASI; Hurtmans et al., 2012), from the Université Libre de Bruxelles (ULB) and the Laboratoire Atmosphères, Milieux, Observations Spatiales (LATMOS). This approach uses pre-calculated lookup tables of absorbance cross sections at various pressures and temperatures, and an optimal estimation method for the inverse scheme. The algorithm derives vertical profiles of CO, on a grid of 18 equidistant layers of 1 km of depth from the surface up to 18 km, and a unique layer from 18 to 60 km. The IASI/MetOp-B CO product including total and partial columns of CO derived by profile integrations, averaging kernels, error estimations and quality flags is publicly available on the French data centre AERIS (https://iasi.aeris-data.fr, last access: November 2024). The product is averaged over a regular horizontal grid of 1° × 1° and CO concentrations are calculated as an average CO volume mixing ratio in ppb within the layer in the same way as far IASI+GOME2 ozone.

2.2 Atmospheric chemistry reanalyses

The global atmospheric chemistry reanalysis products compared in this paper, the Tropospheric Chemistry Reanalysis version 2 (TCR-2) and the Copernicus Atmosphere Monitoring Service reanalysis (CAMS reanalysis), are listed in Table 1. The general configuration of the various data assimilation systems is provided in the following subsections. We regrid these

atmospheric chemistry reanalysis products to 1° × 1° resolutions for consistency with gridded IASI+GOME2 ozone data. Then, we convert their pressure levels to altitude by using geopotential fields from ERA5 (Sect. 2.4).

Table 1: Overview of the global atmospheric chemistry reanalysis products in 2017.

	TCR-2	CAMS reanalysis
Available period	2005–2021	2003–present
Spatial resolution	1.1° × 1.1°	0.7° × 0.7°
Vertical levels (top pressure level)	32 layers (4.4 hPa)	60 layers (0.1 hPa)
Output frequency	2 h (surface) 6 h (3D)	3 h
Meteorological fields	ERA-Interim	ERA-5
Anthropogenic emissions	HTAPv2	MACCity
Biomass burning emissions	GFEDv4	GFASv1.2
Biogenic emissions	Guenther et al. (2006)	Calculated by the MEGAN
Lightning emission	Convective cloud top (Price and Rind, 1992)	Convective precipitation (Meijer et al., 2001)
Data assimilation scheme	EnKF	4D-Var
Assimilated ozone retrievals for 2017	TES, MLS	MLS, OMI, GOME-2, SBUV/2
Assimilated CO retrievals for 2017	MOPITT	MOPITT

155

2.2.1 Tropospheric Chemistry Reanalysis version 2 (TCR-2)

TCR-2 (Miyazaki et al., 2019) is a global atmospheric chemistry reanalysis based on the MIROC-CHASER (Model for Interdisciplinary Research on Climate-Chemical atmospheric general circulation model for study of atmospheric environment and radiative forcing, Watanabe et al., 2011) by the National Aeronautics and Space Administration (NASA) Jet Propulsion
160 Laboratory (JPL) (Miyazaki et al., 2020). TCR-2 uses an ensemble Kalman filter (EnKF) data assimilation technique to combine satellite observations of ozone, CO, nitrogen dioxide (NO_2), nitric acid (HNO_3) and sulphur dioxide (SO_2). TCR-2 has a T106 horizontal resolution (0.7° × 0.7°) with 32 vertical levels from surface to 4.4 hPa. TCR-2 is available at 2-hour intervals for surface concentrations and at 6-hour intervals for 3-D concentrations. Meteorological fields used by TCR-2 are nudged towards the 6-hourly ERA-Interim (Dee et al., 2011). A priori surface emissions from anthropogenic sources are
165 obtained from the HTAP version 2 for 2010 (Janssens-Maenhout et al., 2015). For biomass burning emissions, the monthly Global Fire Emissions Database (GFED) version 4 (Randerson et al., 2018) are used. Emissions from soils are based on

monthly mean Global Emissions Inventory Activity (GEIA) (Yienger and Levy, 1995). Biogenic emissions from vegetation are considered for non-methane hydrocarbons (NMHCs) based on Guenther et al. (2006). Lightning NO_X (LNO_X) sources were simulated by using the convection scheme of MIROC-AGCM (Miyazaki et al., 2017). The global distribution of the flash rate was parameterized for convective clouds based on the relationship between lighting activity and cloud top height (Price and Rind, 1992). The vertical profile of the LNO_X sources were determined on the basis of the C-shape profile, which peaks at the surface and in the upper troposphere, given by Pickering et al. (1998). In the present study, we use 2-hourly ozone and CO TCR-2 data (Miyazaki, personal communication, 2020).

2.2.2 Copernicus Atmosphere Monitoring Service reanalysis (CAMS reanalysis)

CAMS reanalysis is a global atmospheric chemistry reanalysis based on the Integrated Forecast System (IFS) cycle 42R1 by the European Centre for Medium-Range Weather Forecasts (ECMWF) (Inness et al., 2019, last access: 12 April 2022). CAMS reanalysis uses the four-dimensional variational (4D-Var) data assimilation technique to combine satellite observations of ozone, CO, NO_2 and aerosol optical depth (AOD). The spatial resolution of CAMS reanalysis is a reduced Gaussian grid at a spectral truncation of T255, which is equivalent to grid spacing of approximately 80 km globally ($0.7° \times 0.7°$), with 60 vertical levels from surface to 0.1 hPa. CAMS reanalysis is available at 3-hour intervals. Daily global biomass burning emissions are provided by the Global Fire Assimilation System (GFAS) version 1.2 (Kaiser et al., 2012). Anthropogenic emissions are from the MACCity inventory (Granier et al., 2011), with modifications to increase wintertime road traffic emissions over North America and Europe following the correction of Stein et al. (2014). Monthly mean biogenic emissions are calculated offline by the Model of Emissions of Gases and Aerosols from Nature (MEGAN, Guenther et al., 2006) that used meteorological fields from the MERRA-2 following Sindelarova et al. (2014). Natural emissions from soils and oceans are taken from the Precursors of ozone and their effects in the Troposphere (POET) database (Granier et al., 2005; Olivier et al., 2003). LNO_X emissions are simulated by the modules for atmospheric composition in the IFS, named Composition-IFS (C-IFS) (Flemming et al., 2015). The C-IFS has two options to simulate the flash-rate densities using the following input parameters: (i) convective cloud height (Price and Rind, 1992) or (ii) convective precipitation (Meijer et al., 2001). Flemming et al. (2015) showed the comparison of the annual flash rate density from the IFS input data using the parameterisation by Price and Rind (1992), Meijer et al. (2001) and observations. The smaller land–sea differences of Meijer et al. (2001) agreed better with the observations. The observed maximum over central Africa was well reproduced by both parameterisations, while an exaggerated maximum was remarked over tropical South America. In the IFS, LNO_X emissions uses the parameterisation of Meijer et al. (2001) based on convective precipitation. The vertical profile of the LNO_X sources were determined on the basis of the backward C-shape profile, which locates most emission in the middle of the troposphere, given by Ott et al. (2010).

2.3 Observations used for evaluation

2.3.1 The Atmospheric Tomography Mission (ATom)

The Atmospheric Tomography Mission (ATom) is a NASA Earth Venture airborne field campaign to study the impacts of human-produced air pollution on greenhouse gases and on chemically reactive gases over the Pacific and Atlantic oceans along a global-scale circuit (Thompson et al., 2022). ATom consists of four series of flights from ~82° N to ~86° S by using the long-range NASA DC-8 research aircraft. During these flights, the DC-8 repeatedly ascended and descended between ~0.2 and ~13 km in altitude. The four ATom circuits occurred in July–August 2016 (ATom-1), January–February 2017 (ATom-2), September–October 2017 (ATom-3), and April–May 2018 (ATom-4).

The ATom dataset includes merged data from all instruments (Wofsy et al., 2018) provided by the Oak Ridge National Laboratory Distributed Active Archive Center (ORNL DAAC, last access: 24 March 2023). We use ozone, CO, water vapor (H_2O), hydrogen cyanide (HCN), tetra chloroethylene (C_2Cl_4) and NO_X observations. The measurement methods of these tracers are described in detail elsewhere (Bourgeois et al., 2021).

We quantify the influence of biomass burning emission on the tropospheric ozone during ATom-2 and 3 according to the method of Bourgeois et al. (2021). The authors analyse in situ measurements of ozone (O_3) and H_2O, for defining air parcels with $O_3/H_2O > 1$ ppbv ppmv^{-1} and with $O_3/H_2O < 0.003$ ppbv ppmv^{-1} as strongly influenced by stratospheric air and by marine air, respectively. To quantify the respective influence of biomass burning and urban emissions on each air parcel, they use a pair of HCN (biomass burning tracer) and C_2Cl_4 (urban tracer). These two tracers are chosen because their lifetime is similar to that of CO (being between three and five months for these three tracers), and they have been used as a tracer in the previous literature. First, all sampled air masses are classified into four categories. For the region (40° S–40° N), air parcels are either defined as urban air (urban tracer > regional median, biomass burning tracer < regional median), biomass burning air (biomass burning tracer > regional median, urban tracer < regional median), mixed pollution air (both urban and biomass burning tracers > regional median), and well-mixed and aged air (both urban and biomass burning tracers < regional median) corresponding to rather clean or background conditions. The normalized excess mixing ratio (NEMR) of biomass burning and urban tracers is calculated according to following Eq. (1):

$$NEMR_X = \Delta X/\Delta CO, \quad (1)$$

where $NEMR_X$ is the normalized excess mixing ratio of compound X (i.e., X = HCN or C_2Cl_4) to CO, and ΔX (ΔCO) is the difference between the mixing ratio of compound X (CO) and its background level. The background levels are defined as the average mixing ratio in well-mixed and aged air masses. The respective influence of urban and biomass burning emissions (F_X) is then calculated as the ratio of the NEMR of compound X to the average emission ratio of compound X (ER_X) as follows:

$$F_X = NEMR_X/ER_X, \quad (2)$$

Bourgeois et al. (2021) use 5.7 pptv ppbv^{-1} (HCN/CO) and 0.03 pptv ppbv^{-1} (C_2Cl_4/CO) as ERs of biomass burning and urban air according to Andreae (2019) and Kondo et al. (2004). Then, tropospheric ozone attributed to biomass burning and urban emissions are calculated as follows:

$$O_3^X = F_X \times \Delta O_3, \quad (3)$$

A dataset containing back trajectories and boundary layer influences of air parcels along the ATom flight tracks is also distributed by the ORNL DAAC (Ray, 2021, last access 22 December 2023). We use the back trajectories interpolated by using National Centers for Environmental Prediction (NCEP) Global Forecast System (GFS) meteorology. Model trajectories are initialized at receptors spaced 1 min apart along the ATom flight tracks, followed backwards for 30 days, and reported at 3-hour resolution. We also use average probability of boundary layer influence in the dataset to identify air masses influenced by lightning (Sect. 3.4). Boundary layer influences are determined based on the location of these air masses along 30-day back trajectories.

2.4 Meteorological data

Meteorological conditions leading to photochemical production of ozone and transport are described with the ERA5 reanalysis (Hersbach et al., 2020) produced by the European Centre for Medium-Range Weather Forecast (ECMWF). We use meteorological fields with global coverage, a horizontal resolution of 0.25° × 0.25°, 37 pressure levels, and a time step of 1 hour. Eastward and northward components of wind, vertical velocity, relative humidity, geopotential, and potential vorticity are used to describe transport patterns downloaded from the Climate Data Store (https://cds.climate.copernicus.eu/, last access: 19 December 2023).

The NO_X production by lightning is generally represented by parameterizations in global chemistry transport models, resulting in differences between models and thus uncertainties. Scientific observations of lightning occurrence have been recorded from the space and the ground. The Lightning Imaging Sensor – Optical Transient Detector (LIS/OTD) dataset by two lightning detection sensors: the OTD on the Orbview-1 satellite and the LIS aboard the Tropical Rainfall Measuring Mission (TRMM) satellite has been most widely used. However, the LIS/OTD 0.5 Degree High Resolution Monthly Climatology (HRMC) covers the period 1995–2014, and is neither updated (Cecil et al., 2014). The World Wide Lightning Location Network (WWLLN) is a global network monitoring lightning activity by very low frequency radio sensors (Dowden et al., 2002). Recently, a global, high-resolution gridded time series and climatology of lightning stroke density, the WWLLN Global Lightning Climatology (WGLC) has been published (Kaplan and Lau, 2021a) and is freely available at 0.5° and 5 arcmin spatial with daily and monthly temporal resolution (Kaplan and Lau, 2021b, last access: 19 April 2023). Kaplan and Lau (2021a) compared climatological mean annual lightning density between the WGLC and the LIS/OTD, even though the periods of the record are not overlapping and the lightning phenomenon observed, i.e., strokes in the WGLC and flashes in the LIS/OTD, is different. The LIS/OTD captured more lightning than the WGLC, particularly over land. The area of the greatest difference was in the eastern Congo Basin, this was also a hotspot for lightning in the WGLC. Other regions where the WGLC

had lower lightning than the LIS/OTD were in the Western High Plateau of Cameroon and northwestern South America. In the Northern Hemisphere and over the oceans, the differences were smaller.

As a convective proxy, we use monthly outgoing longwave radiation (OLR) data distributed by the National Oceanic and Atmospheric Administration (NOAA) Physical Science Laboratory (PSL) (Liebmann and Smith, 1996; https://psl.noaa.gov/, last access: 10 March 2023). The OLR is a good indicator of the position of the ITCZ. Deep convective clouds present at the ITCZ are associated with OLR below 220 W m^{-2} (e.g. Park et al., 2007).

2.5 Other data

The locations of fires are derived from the Terra and Aqua MODIS (Moderate Resolution Imaging Spectrometer) active fire products (MCD14ML Collection 6; Giglio et al., 2016) distributed by the Fire Information for Resources Management System (FIRMS; https://firms.modaps.eosdis.nasa.gov/, last access: 13 March 2020). This dataset provides the values of fire radiative power (FRP) and the inferred hotspot type: "presumed vegetation fire", "active volcano", "other static land source", and "offshore". We only use the FRP values of presumed vegetation fire with a confidence level greater than 50 %.

3 Results and discussion

The analysis of the distribution and origins of tropospheric ozone over the Tropical Atlantic is presented here in two steps. First, in Sect. 3.1, we analyse the monthly evolution of key elements that influence ozone distribution, namely tropical convective activity described by lightning and biomass burning emissions estimated by fire detections. We also quantify the differences between several tropospheric ozone products (from models and satellite observations) to identify the period with the largest uncertainties. This leads to a more detailed description of the tropospheric ozone distribution in one of the months with the largest uncertainties (February) and in one of the months with the smallest uncertainties (October).

The following Sect. 3.2, 3.3 and 3.4 looks in detail at the distribution of tropospheric ozone and carbon monoxide, an ozone precursor derived from combustion and thus used to identify the air mass origin of either biomass fires or anthropogenic activities. This is done with coincident in situ and satellite measurements and reanalysis during the periods 13–15 February and 17–20 October 2017. This section is followed by a detailed description of the origins of tropospheric ozone and its precursors, including an explanation of the gaps between observational (both in situ and satellite) and modelling (atmospheric chemistry reanalysis) data sets.

3.1 Monthly evolution of tropospheric ozone and related variables over the Tropical Atlantic

The climate in the tropics is characterised by alternating wet and dry seasons depending on the position of the ITCZ. It moves north in the Northern Hemisphere summer and south in the Northern Hemisphere winter. Lannuque et al. (2021) defined two main seasons (from December to March and from June to October) and two transition seasons (from April to May and

November) in the African inter-tropical zone based on the position of ITCZ, defined by zonal and meridional winds and relative humidity because the classical four seasons were not adapted to their study area.

According to the maps presented in Fig. S2–S3, lightning and fire activities can be observed throughout the year in both, the African and the South American continents, with large seasonal variability, clearly associated with the ITCZ annual shift. Estimations of the regional lightning source altitudes by the satellite (derived by Peterson 2022) suggest that the source altitude distributions peak at 10–11 km altitude over the Amazon and the Congo Basins. In the La Plata Basin and South Africa, they peak at lower altitude. Therefore, wind vectors at 10 km of altitude are presented in Fig. S2 and 1a–b. In February, the highest lightning densities are observed in the Gulf of Guinea, Central and Southern Africa, and over South America (Fig. S2a). This clearly shows that this is the location where strong ascending motions within the troposphere are expected, which may bring air pollutants emitted from the surface such as ozone precursors up to the middle and upper troposphere. In May, convective activity shifts northwards in location as suggested by the decrease of lightning in South America and peaks over Colombia and Venezuela (Fig. S2b) and an increase over the African Sahel in a vast west-to-east band. While lightning density distribution in August is quite similar to the previous month, the density decreases in Western Africa (Fig. S2c). In November, the centre of lightning activities moves southwards as a consequence of the ITCZ shift (Fig. S2d). The highest lightning densities are detected in the Congo Basin, Brazil, Northern and Western South America. In this period (May–August), deep convection likely affects atmospheric circulation mainly north of the equator.

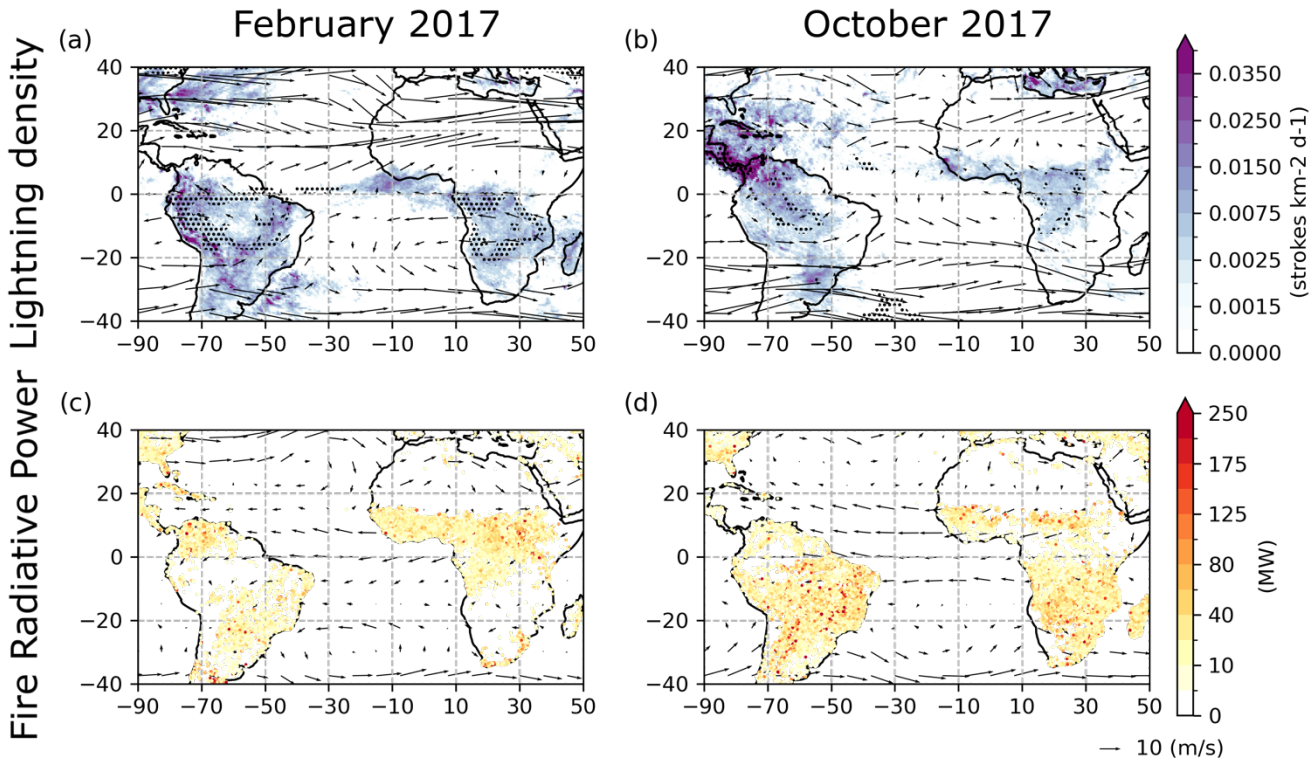

Figure 1: Monthly WGLC lightning density and fire radiative power (FRP) of presumed vegetation fire in (a and c) February and (b and d) October 2017. Winds at 3 and 10 km of altitude from ERA5 are indicated by black arrows in February and October, respectively. Black dots (a–b) indicate areas with OLR < 220 W m^{-2}.

According to FRP maps presented in Fig. S3, fire activity also varies with the ITCZ annual shift. In February, enhancement of FRP can be observed in the Caribbean North, Southern Cone, Western and Central Africa (Fig. S3a). Following the wind flow (shown at 3 km of altitude in Fig. S3), trace gases and smoke emitted by biomass fires are then expected to largely affect the Tropical Atlantic. In May, while the location of the highest FRP values is similar to previous months, the intensity decreases in South America and the Sahel south of the Sahara Desert, and increases in the Congo Basin (Fig. S3b). In August, the fire intensity is the highest over the Congo Basin and Brazil (Fig. S3c). In November, fires are still detected in South America and Southern Africa, and restarts over the Sahel south of the Sahara Desert (Fig. S3d). This is consistent with previous studies suggesting that the peak of burning events over Africa north of the equator occurs in January, whilst south of it in July (Roberts et al., 2009). May and October are expected to be the periods of transition between hemispheres. Consistency is also found

over South America, where biomass burning emissions start increasing in June, enhance in July and August, and peak in September, and start decreasing in October (Pereira et al., 2022).

There are strong seasonal variations in the location of fires and deep convection, and consequently, change in the regime of atmospheric composition, for instance tropospheric ozone, is large over the Tropical Atlantic. Given these complex conditions over this remote area, we start our analysis with an initial estimate of the uncertainties of atmospheric modelling of tropospheric ozone as regional SD between several atmospheric chemistry reanalyses and satellite measurements. Moreover, a large variability of tropospheric ozone abundance is reported in this area (Thompson et al. 2021). While the ozone minima is seen in January through April or May, its maximum occur largely from imported biomass burning air masses at 6–8 km from September to November (based on SHADOZ records from the surface to 20 km between Natal, Brazil (5.4° S, 35,4° W) and Ascension Island, the United Kingdom (8.0° S, 14.4° W)).

We consider monthly averaged horizontal distributions of ozone in the lowermost troposphere (defined here as the atmospheric layer between the surface and 3 km above sea level) over the Tropical Atlantic (25° S–25° N, 34° W–18° W, within the black rectangle in Fig. 2g–h and Fig. 3g–h). According to Figure S4, monthly variation of average ozone shows clear seasonality with two maxima from September to October and in March. The maxima of average ozone correspond to the two biomass burning seasons over Africa. The relative scatter of the values of ozone abundance between the three products (TCR-2, CAMS reanalysis and IASI+GOME2) can be expressed as a coefficient of variation (CV) defined as the ratio of SD to mean ozone. Monthly variation of CV show different seasonality with two maxima from November to March and June, and with two minima in May and from August to October. The highest average ozone (~38 ppb) and small CV (~10%) can be observed in October, corresponding to the biomass season in the Southern Hemisphere (Fig. 1d). The second largest CV (~22 %) can be observed in February, corresponding to the biomass burning season in the Northern Hemisphere and deep convection over Central Africa and the Gulf of Guinea (Fig. 1a and c).

A previous intercomparison of four chemistry reanalyses including TCR-2 and CAMS reanalysis, suggests the largest SD at 850 hPa over South America, Central Africa, and Northern Australia (Huijnen et al. 2020). This is mainly associated with the differences of the representation of biomass burning emissions and its impact on ozone production among the systems. Estimates of CO emissions for African fires have been subject to considerable uncertainty because of the high variability of African fires in time and space (Andela and van der Werf, 2014). Two chemistry reanalysis products used in this study adopt different biomass burning emission inventories (Table 1). GFED used by TCR-2 is produced by using the bottom-up approach which uses burned area and fuel loads (van der Werf et al., 2017). GFAS (used by CAMS reanalysis) is produced by using the top-down approach which uses FRP data (Kaiser et al., 2012). Mismatches between bottom-up and top-down approaches have been discussed in previous studies (e.g., Stoppiana et al., 2010; van der Werf et al., 2006; Zheng et al., 2018). Evaluations of uncertainties of fire emissions and their impact on the ozone production are beyond the scope of this study.

Figure 2 shows horizontal distributions of monthly mean ozone and the CV in the lowermost troposphere in February and October 2017, within the period shown from Fig. S4 as that with the largest and the smallest differences. In February 2017, the IASI+GOME2, TCR-2 and CAMS reanalysis products show high concentrations of ozone from Western Africa to the Gulf

of Guinea (Fig. 2a, c and e). An enhancement of ozone in the north of the St. Helena anticyclone between 10° S and 20° S and centred at 20° W can be only observed by IASI+GOME2, whereas two chemistry reanalysis products show low ozone values below 20 ppb. TCR-2 and CAMS reanalysis show relatively higher concentration of ozone over the Atlantic in the Northern Hemisphere as compared to IASI+GOME2. CV is small in the active fire region over Western Africa (Fig. 2g). It means that differences of ozone concentration among the datasets is small relative to their concentration. Large CV can be seen in the outflow from Western Africa over the Tropical Atlantic, which may be associated with differences of the representation of transport and convection. Also, large CV can be seen in the north of the St. Helena anticyclone as enhancement of ozone is only observed by IASI+GOME2, and in Brazil and Southern Africa as low ozone concentration is observed by CAMS reanalysis. In addition, moderate CV can be also seen over the North Atlantic between 10° N and 40° N as two reanalyses show higher ozone concentration than that of IASI+GOME2.

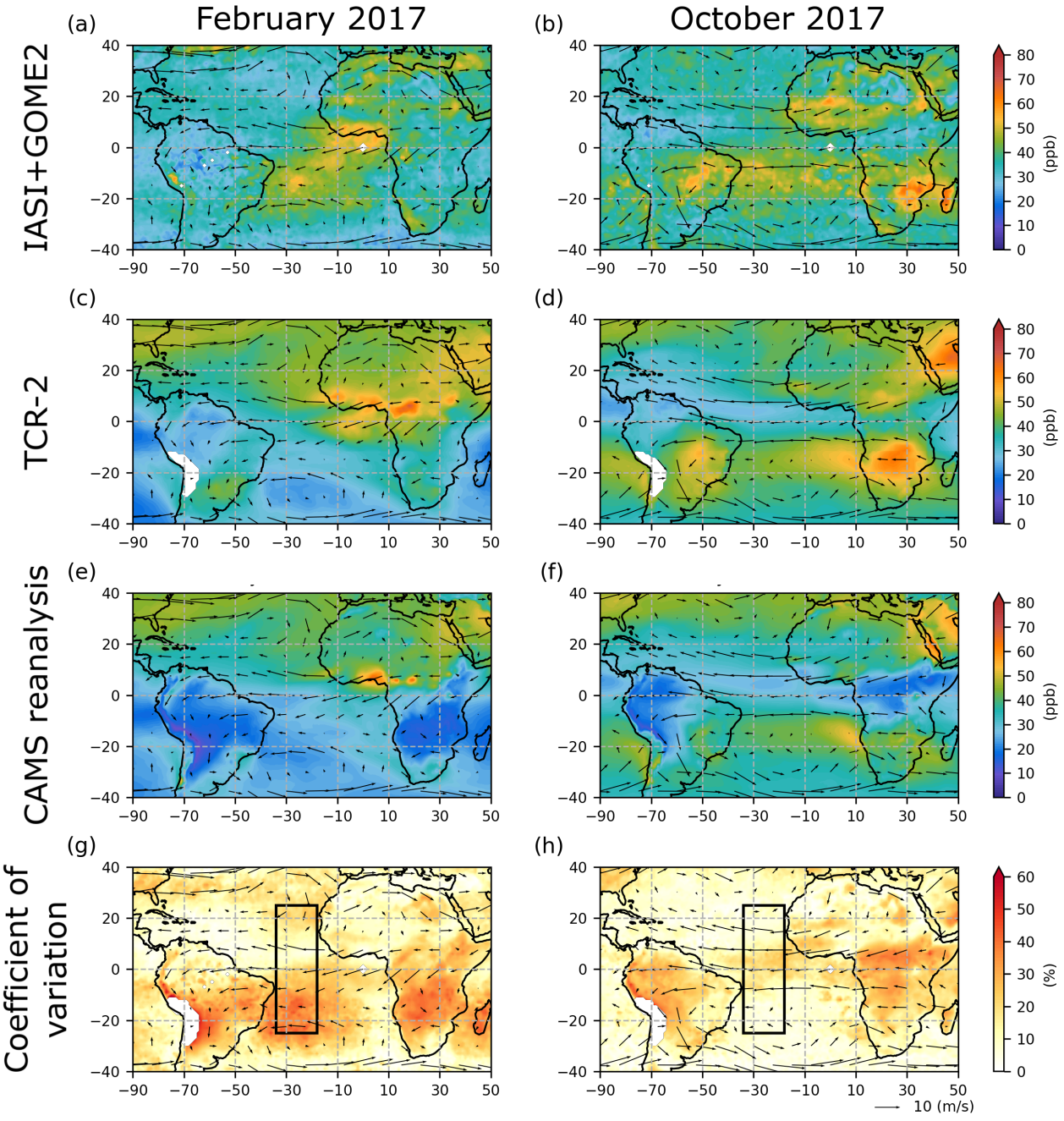

Figure 2: Distribution of monthly mean ozone from surface to 3 km in February and October 2017. (a and e) IASI+GOME2, (b and f) TCR-2, (c and g) CAMS reanalysis and (d and h) coefficient of variation . Winds at 3 km altitude from ERA5 are indicated by black arrows. Black rectangle indicates the region to calculate average ozone and coefficient of variation in Fig. S4 (25° S–25° N, 34° W–18° W).

In October 2017, all products show high concentrations of ozone in the Congo Basin, Brazil and the outflow over the South Atlantic in the lowermost troposphere (Fig. 2b, d and f). We can also see moderate enhancement of ozone in south of the Sahara Desert. The distribution of ozone is consistent with the location of the regions with large fire activity (Fig. 1d). Large CV can be seen over the Amazon Rainforest, Central Africa and the Tropical Atlantic (Fig. 2h). In these regions, CAMS reanalysis shows lower ozone concentration than the other two datasets (Fig 2f).

IASI+GOME2 shows lower ozone concentration as compared to two reanalysis products in the atmospheric layer between 6 km and 9 km above sea level (Fig. 3). In February 2017, a rather different situation is seen for ozone distribution depicted in the middle troposphere. All products show a horseshoe-shaped structure of high concentration of ozone from Southern and Western Africa to the east of Brazil. Large CV can be seen over Southern Africa, the Amazon Rainforest and the Atlantic in the Northern Hemisphere (Fig. 3g). In October 2017, all products show high concentrations of ozone in the Congo Basin, Brazil and the outflow over the South Atlantic. Relatively large CV can be seen in the Northern Hemisphere (Fig. 3h). The next sections discuss in detail these differences and compares them with in situ reference measurements performed by an aircraft during 13–15 February and 17–20 October 2017.

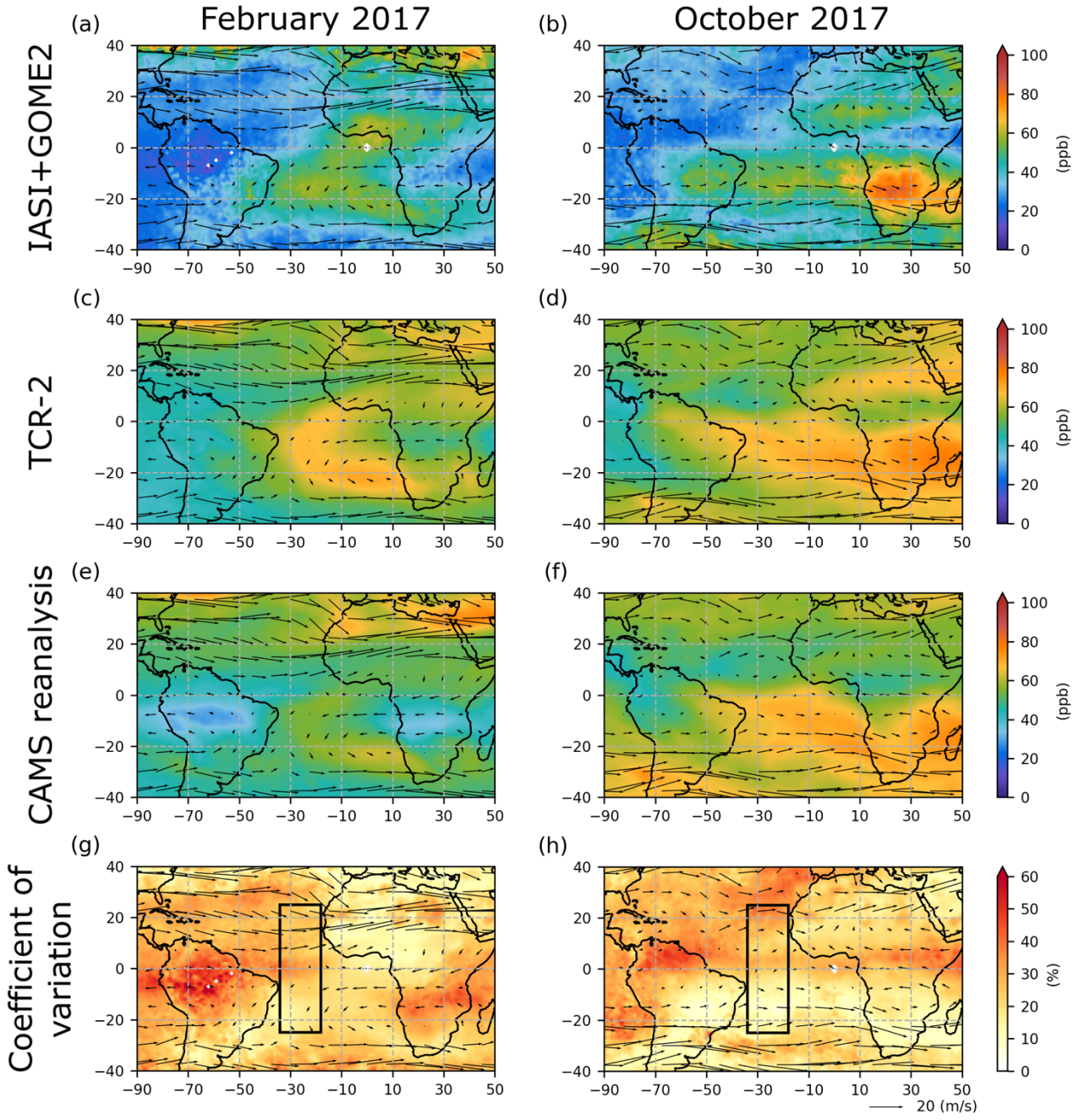

Figure 3: Distribution of monthly mean ozone from 6 km to 9 km in February and October 2017. (a and e) IASI+GOME2, (b and f) TCR-2, (c and g) CAMS reanalysis, and (d and h) coefficient of variation . Winds at 9 km altitude from ERA5 are indicated by black arrows. Black rectangle indicates the region to calculate average ozone and coefficient of variation in Fig. S4 (25° S–25° N, 34° W–18° W).

3.2 Tropospheric ozone spatial distributions during Atom campaign

In order to better understand the differences between atmospheric chemistry reanalyses and satellite observations, we focus here on the periods and locations of ATom-2 and Atom-3 in situ observations of tropospheric ozone and CO in February and October 2017. The NASA DC-8 aircraft transect over the Atlantic on 13 and 15 February 2017 covers from south to north, respectively, from 53° S to 8° S and from 8° S to 39° N (on each of these days, see the flight track on the left panels of Figs. 4 and 5). On 17, 19 and 20 October 2017, the transect covers from 53°S to7°S, from 7°S to 16°N and from 9°N to 39°N (see the flight track on the right panels of Figs. 4 and 5). Therefore, we consider here concentrations of the three products (IASI+GOME2, TCR-2 and CAMS reanalysis) averaged for the periods from 13 to 15 February and from 17 to 20 October 2017.

Panels on the left of Figs. 4 and 5 shows horizontal distributions of ozone for the period from 13 to 15 February 2017. These ozone distributions are generally similar to the monthly mean distributions on the left panels of Fig. 2 and 3. In the lowermost troposphere, all products show enhancement of ozone concentrations over active biomass burning areas near the coast of the Gulf of Guinea and over the nearby Sea following the wind flow. Only IASI+GOME2 shows high ozone concentration (> 50 ppb) in the north of St. Helena anticyclone (centred at 30° S, 40° W). TCR-2 and CAMS reanalysis show relatively higher concentration in the Northern Hemisphere as compared to IASI+GOME2. In the middle troposphere, as at the lowermost troposphere, similar distributions are found with respect to monthly averages. All products show the previously remarked ozone plume forming a horseshoe-shape from Southern Africa to the east of Brazil (20° S) and until the Gulf of Guinea. Especially, ozone concentrations from TCR-2 are the highest ones over the South Atlantic (about 80 ppb). IASI+GOME2 shows lower concentration as compared with two reanalyses.

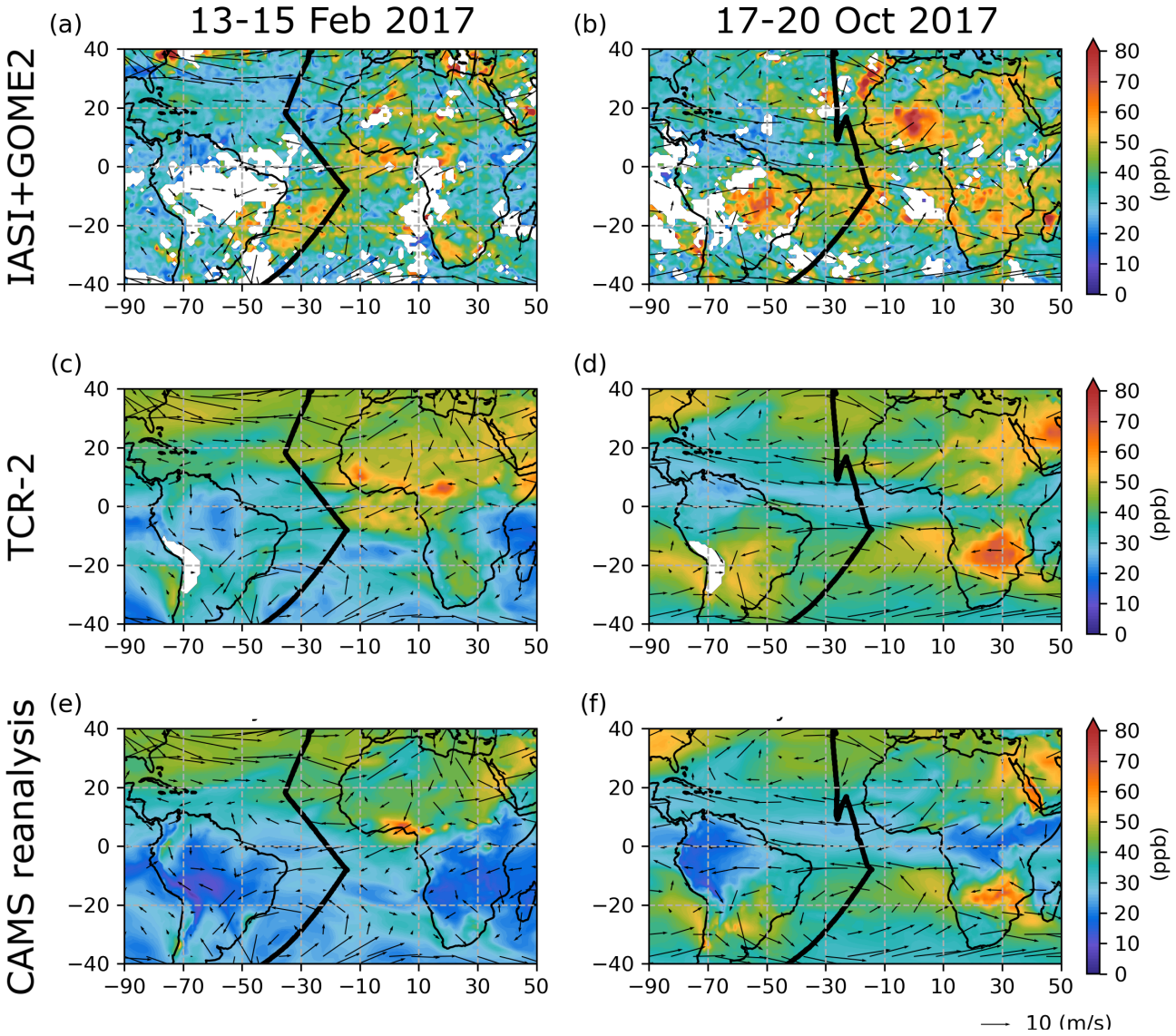

Figure 4: Distribution of mean ozone from surface to 3 km during 13–15 February and 17–20 October 2017. Black bold lines in (a–b) IASI+GOME2, (c–d) TCR-2 and (e–f) CAMS reanalysis indicate the ATom-2 and Atom-3 flight tracks. Winds at 3 km altitude from ERA5 are indicated by black arrows.

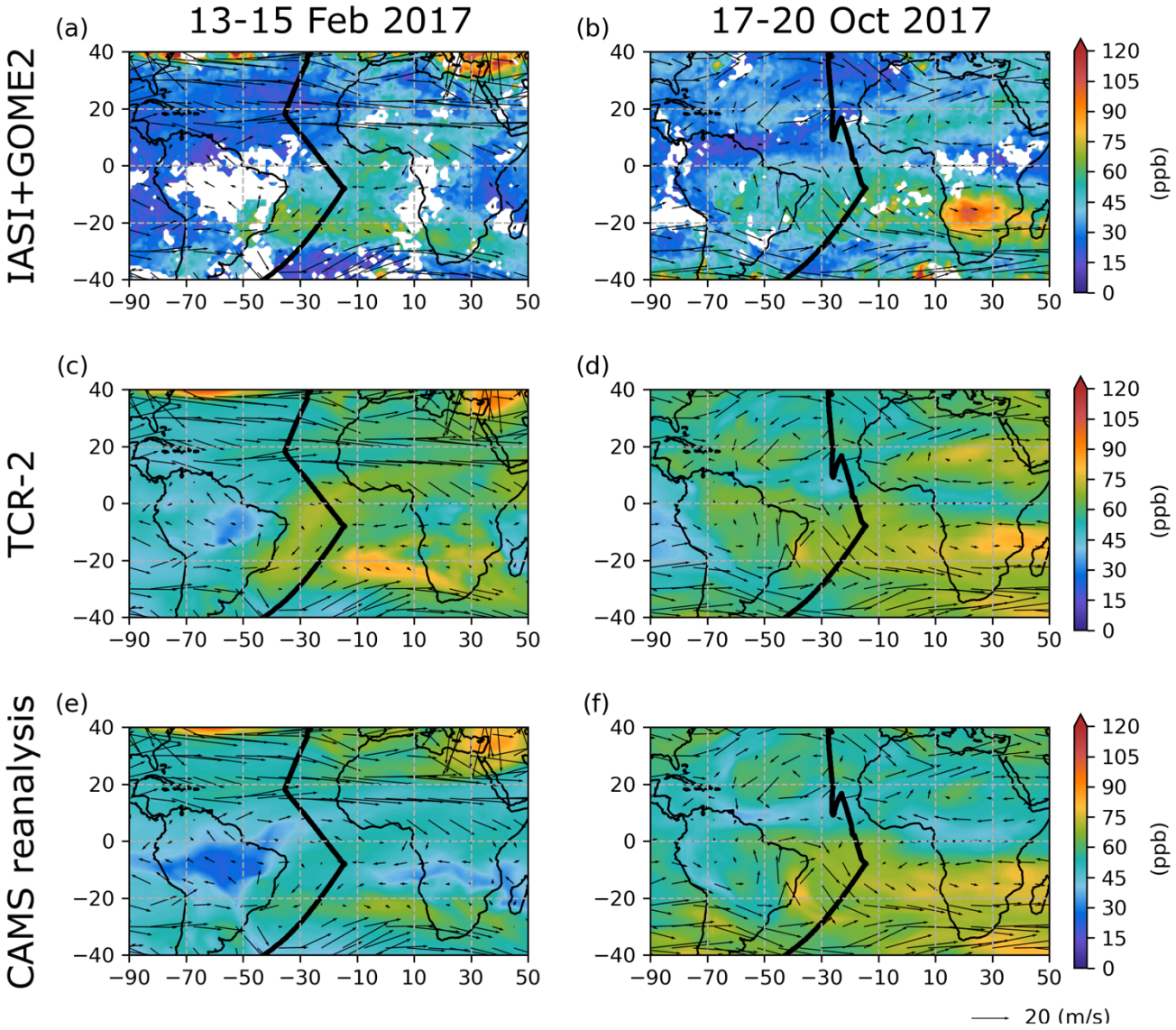

Figure 5: Distribution of mean ozone from 6 km to 9 km during 13–15 February and 17–20 October 2017. Black bold lines in (a–b) IASI+GOME2, (c–d) TCR-2 and (e–f) CAMS reanalysis indicate the ATom-2 and Atom-3 flight tracks. Winds at 9 km altitude from ERA5 are indicated by black arrows.

Panels on the right of Fig. 4 and 5 shows horizontal distributions of ozone for the period from 17 to 20 October 2017. These ozone distributions are also generally similar to the monthly mean distributions on the right hand-side of Fig. 2 and 3. In the lowermost troposphere, all products show enhancement of ozone concentrations over active biomass burning areas in Southern

Africa and Brazil. Only IASI+GOME2 shows high ozone concentration (> 60 ppb) over Western Africa (Fig. 4b). In the middle troposphere, as at the lowermost troposphere, similar distributions are found with respect to monthly averages. All products show high concentrations of ozone in the Congo Basin, Southern Brazil and the outflow over the South Atlantic. Moderate enhancement of ozone can be seen over the African Sahel. IASI+GOME2 shows lower concentration as compared with two reanalyses. The overall similarities between the ozone concentrations during 13–15 February and 17–20 October 2017 and the average over the whole month indicate that the aspects studied in the 3-day and 4-day periods, such as the origins of tropospheric ozone (Sect. 3.4), are likely stable features representative of a larger period (at least a month).

3.3. Ozone concentrations in the troposphere

To assess the accuracy of the satellite and reanalysis ozone products, we compare the vertical profiles along the flight track of ATom-2 indicated by bold black line in Figs 4 and 5 (the left panels of Fig. 6). The values are extracted from the grid of the 1° × 1° datasets along the flight track of ATom-2. The ozone distribution of three products is characterized by an ozone plume in the troposphere between 30° S and 5° N below 10 km of altitude. IASI+GOME2 depicts the ozone plume at 3–6 km, which is lower than the altitude of the plume shown by the reanalysis products (the left panels of Fig. 6). This enhancement of ozone concentration in IASI+GOME2 corresponds to the one seen in the lower troposphere horizontal distribution over the South and Tropical Atlantic (Fig. 4a). The horizontal distribution of ozone from the reanalyses presents lower concentrations in the lowermost troposphere between 30° S and 5° N (Fig. 4c and e), as the ozone plume is located at higher altitude (> 5 km) in this case (Fig. 6c and e). Particularly in the Northern Hemisphere (north of 10° N), we can observe large difference of ozone concentration between IASI+GOME2 and two reanalyses (the left panels of Fig. 6). This difference corresponds to concentrations 20 ppb lower for IASI+GOME2 than for the reanalyses. In addition, an enhancement of ozone from the upper troposphere to the middle and lower troposphere can be observed in reanalyses around 25° N. However, IASI+GOME2 shows only an enhancement of ozone concentrations up to 40 ppb in the lower troposphere around 15° N. The satellite-derived vertical profiles do not show larger values until the lower stratosphere.

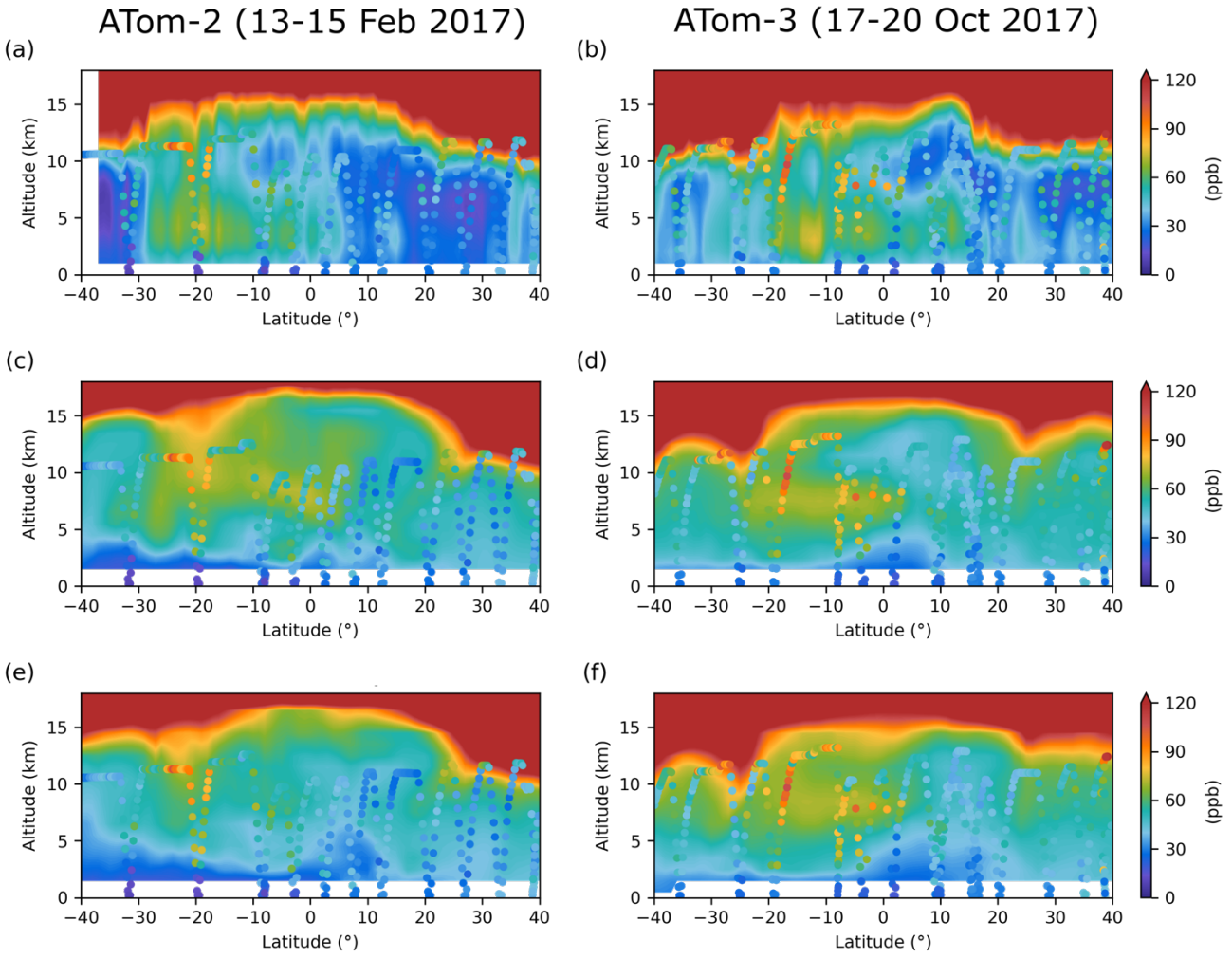

Figure 6: Vertical profiles of ozone concentrations for the periods from 13 to 15 February and from 17 to 20 October 2017. Dots indicate ATom-2 and ATom-3 observations. The ozone concentrations of (a and d) IASI+GOME2, (b and e) TCR-2 and (c and f) CAMS reanalysis are averaged for the period from 13 to 15 February 2017 and from 17 to 20 2017, respectively, and are extracted along the ATom flight tracks.

The transect of ATom-2 in situ measurements and IASI+GOME2 shows a remarkable agreement, across the whole south-north track and within the whole troposphere (Fig. 6a). This agreement is clearly better than with respect to two reanalyses. Both ATom-2 and IASI+GOME2 depict a similar structure of the ozone plume in the troposphere (2 to 7 km of altitude) located between 30° S to 5° N. At about 3 km, ATom-2 ozone concentrations are 68 ppb (20.1° S) and 54 ppb (19.1 °S), near the values depicted by IASI+GOME2 (59–70 ppb between 19° S to 21° S). Lower concentrations are shown by TCR-2 and CAMS reanalysis, respectively of 44–51 ppb and 34–40 ppb. This region is corresponding to the region where only

IASI+GOME2 shows high concentration in the north of St. Helena anticyclone (Figs. 2a and 4a). It suggests that two reanalysis products underestimate the ozone concentration in the lower troposphere at around 20 °S. In the middle troposphere (4–7 km), ATom-2 measure similar ozone levels as both IASI+GOME2 and TCR-2. On the other hand, Atom-2 shows larger concentrations in the upper troposphere at 11 km of altitude (> 90 ppb) than the satellite and the two reanalysis products.

In the Northern Hemisphere (north of 5° N and until 35° N), a clear decrease of ozone concentrations within the troposphere (down to about 30 ppb) is clearly observed by both Atom-2 and IASI+GOME2 (Fig. 6a). On other hand, none of two reanalyses depict such ozone reduction (Fig. 6c and e). A quantitative assessment of the difference in the Northern Hemisphere to evaluate their capability is presented in Table 2. We compare ozone concentrations of three products (IASI+GOME2 and two reanalyses) with ATom-2 between 10° N and 30° N. In the lowermost troposphere, IASI+GOME2 shows lower mean concentration (25.2 ppb) compared to ATom-2 (32.7 ppb), whereas the other reanalysis products show much higher concentrations. Mean ozone concentrations from TCR-2 and CAMS reanalysis are 10–14 ppb higher. We find a robust correlation between IASI+GOME2 and ATom-2 ozone concentrations (R = 0.64, p-value < 0.05). These results suggest that the ozone concentration over the Atlantic in the Northern Hemisphere is overestimated by two chemistry reanalyses in the lower troposphere, while the best agreement with ATom-2 is clearly seen for IASI+GOME2 in correlation and absolute values.

Table 2: Summary ozone statistics for the lower troposphere (0–6 km) along the ATom-2 flight track between 10°N and 30°N. R is correlation coefficient with respect to ATom-2. Asterisk denotes statistical significance at p-value < 0.05 (*) and p < 0.01 (**).

	Atom-2	IASI+GOME2	TCR-2	CAMS reanalysis
0–6 km (number of data = 27)				
Mean	32.7	25.2	46.7	42.8
Median	32.3	24.4	47.6	43.8
SD	5.8	7.3	5.9	4.3
R		0.64**	0.38	0.39*

The ozone distribution of the two reanalysis products is characterized by an ozone plume in the troposphere between 25° S and the equator at 5–10 km of altitude during ATom-3 (see right panels of Fig. 6). IASI+GOME2 depicts the ozone plume at 3–6 km, which is lower than the altitude of the plume shown by the reanalysis products. A moderate enhancement of ozone can be seen in the north of 10 °N. These enhancements of ozone concentration correspond to those seen in the lower troposphere horizontal distribution over the Atlantic (the right panels of Fig. 4). The horizontal distribution of ozone from the reanalyses presents lower concentrations in the lowermost troposphere around the equator (Fig. 4d and f). Particularly in the Northern Hemisphere (north of 15° N), we can observe large difference of ozone concentration between IASI+GOME2 and two reanalyses (the right panels of Fig. 6) just like the case in February 2017. This difference corresponds to concentrations 20 ppb lower for IASI+GOME2 than for the reanalyses. In addition, an enhancement of ozone from the upper troposphere to

the middle and lower troposphere can be observed in reanalyses around 25° N. As compared to the case of ATom-2, the transect of ATom-3 in situ measurements and two reanalysis products shows a remarkable agreement, across the whole south-north track and within the whole troposphere (Fig. 6d and f). ATom-3 and two reanalysis products shows similar ozone concentrations in the Northern Hemisphere. Lower concentrations are shown by IASI+GOME2. Variation of mean ozone concentration over the Tropical Atlantic shows a maximum in October, whereas CV is small (Fig. S4). It means that reanalyses reproduce the distribution of ozone relatively well.

3.3 Carbon monoxide concentrations in the troposphere

Tropospheric ozone is a secondary pollutant, which is both chemically produced and destroyed during the transport in the atmosphere. Therefore, understanding its origin is a complex task. A first analysis of the origin of air masses rich in tropospheric ozone is presented here by investigating the vertical profiles of CO concentrations corresponding to satellite retrievals of CO derived from IASI measurements and CO concentrations derived from the two reanalyses (Fig. 7) in a similar way as done for ozone in the previous subsection (Sect. 3.2). In February 2017, three products are characterized by a maximum of CO abundance around the equator in the lowermost troposphere (the left panels of Fig. 7). This is consistent with Atom-2 measurements of CO. The CO concentrations retrieved by IASI are in good agreement with those measured by ATom-2 (> 250 ppb), which are clearly higher than the CO abundance in the reanalysis products. At about 5° S, the CO maximum underestimated by the two reanalyses are located at 2–3 km of altitude. It is composed of three CO plumes: from surface to the middle troposphere (15° S–15° N), from the middle troposphere to the upper troposphere (25° S–5° N) and in the upper troposphere (10° S–20° N). ATom-2 measurements are consistent with these CO enhancements in the upper and middle troposphere. In addition, all products and ATom-2 measurements show an enhancement of CO in the Northern Hemisphere (north of 20° N).

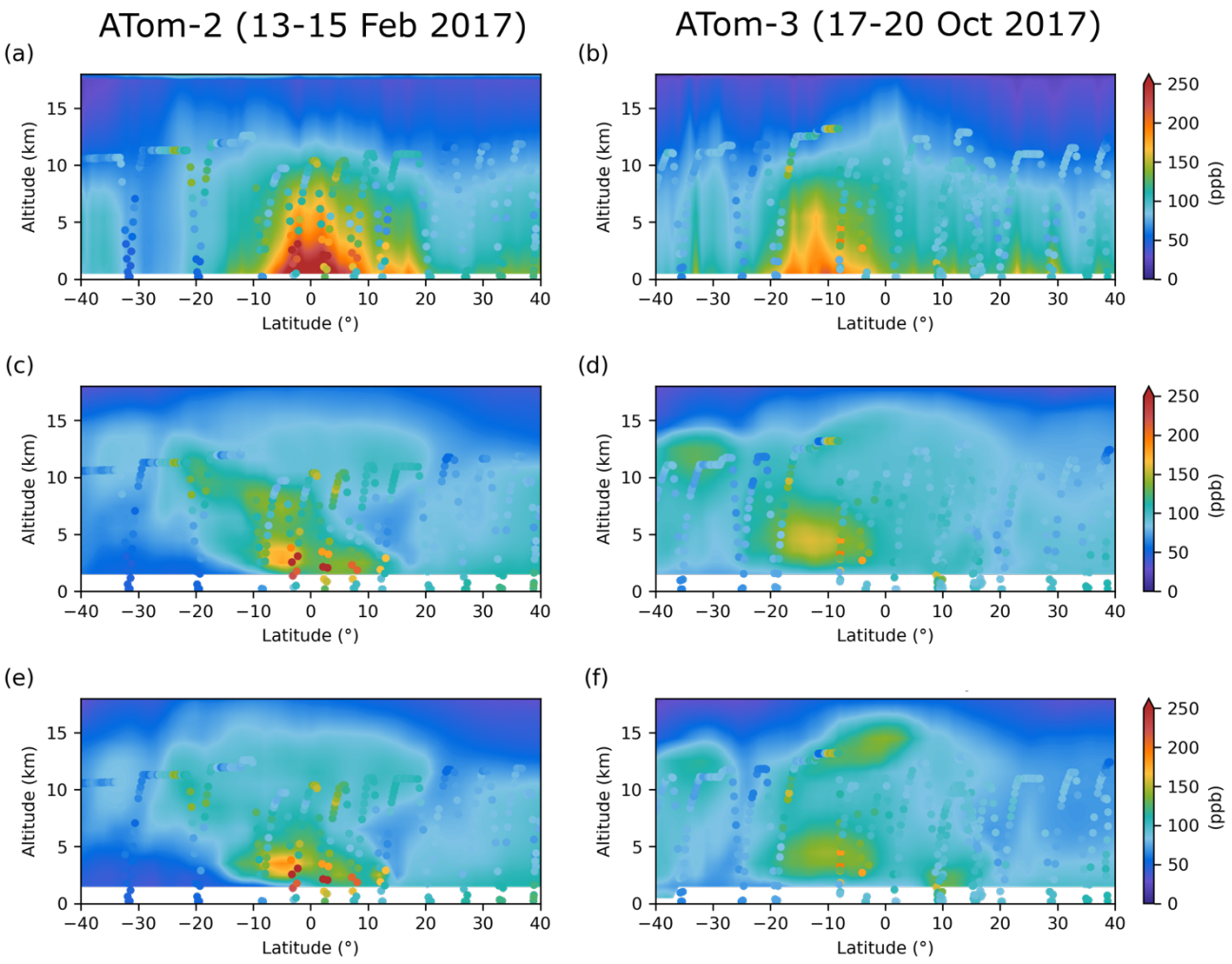

Figure 7: Vertical profiles of CO concentrations for the periods from 13 to 15 February and from 17 to 20 October 2017. Dots indicate ATom-2 and Atom-3 observations. The CO concentrations of (a) IASI, (b) TCR-2 and (c) CAMS reanalysis are averaged for the period from 13 to 15 February 2017 and from 17 to 20 October 2017, respectively, and are extracted along the ATom flight tracks.

Fig. 7 (right panels) shows vertical profiles of CO concentration along the flight track of ATom-3 (indicated in Fig 4 and 5). Three products are characterized by a maximum of CO abundance between 20 °S and the equator in the lower troposphere. At about 20°–10° S, the CO maximum underestimated by the two reanalyses is located at 2–7 km of altitude. IASI might not reproduce the shape of the CO plume. ATom-3 indicates an enhancement of CO in the upper troposphere at about 10° S. IASI+GOME2 and TCR-2 show such enhancement. Only CAMS reanalysis shows this enhancement.

Further insights of the consistence between ATom-2 and the satellite and reanalyses datasets can be analysed from ratios between ozone and CO concentrations (O_3/CO). Enhancements of this ratio along transport suggest ozone photoproduction (e.g. Cuesta et al., 2018), while it may vary between different air masses depending on their origin or other processes affecting its chemical composition. Fig. 8 (left panels) shows vertical profiles of ratio of ozone and CO concentrations along the flight track of ATom-2. Although the vertical sensitivity of IASI differs from that of IASI+GOME2, the corresponding O_3/CO ratio generally shows a good agreement with that of ATom-2 all along the track, over the South, Tropical and North Atlantic between 30° S and 40° N (Fig. 8a). Both in situ measurements and satellite retrievals depict high values near 1 over the South Atlantic (30° S to 20° S) below 10 km of altitude. North of this area (5° S–35° N), lower values of the ratio between 0.2 and 0.4 are consistently shown by both datasets.

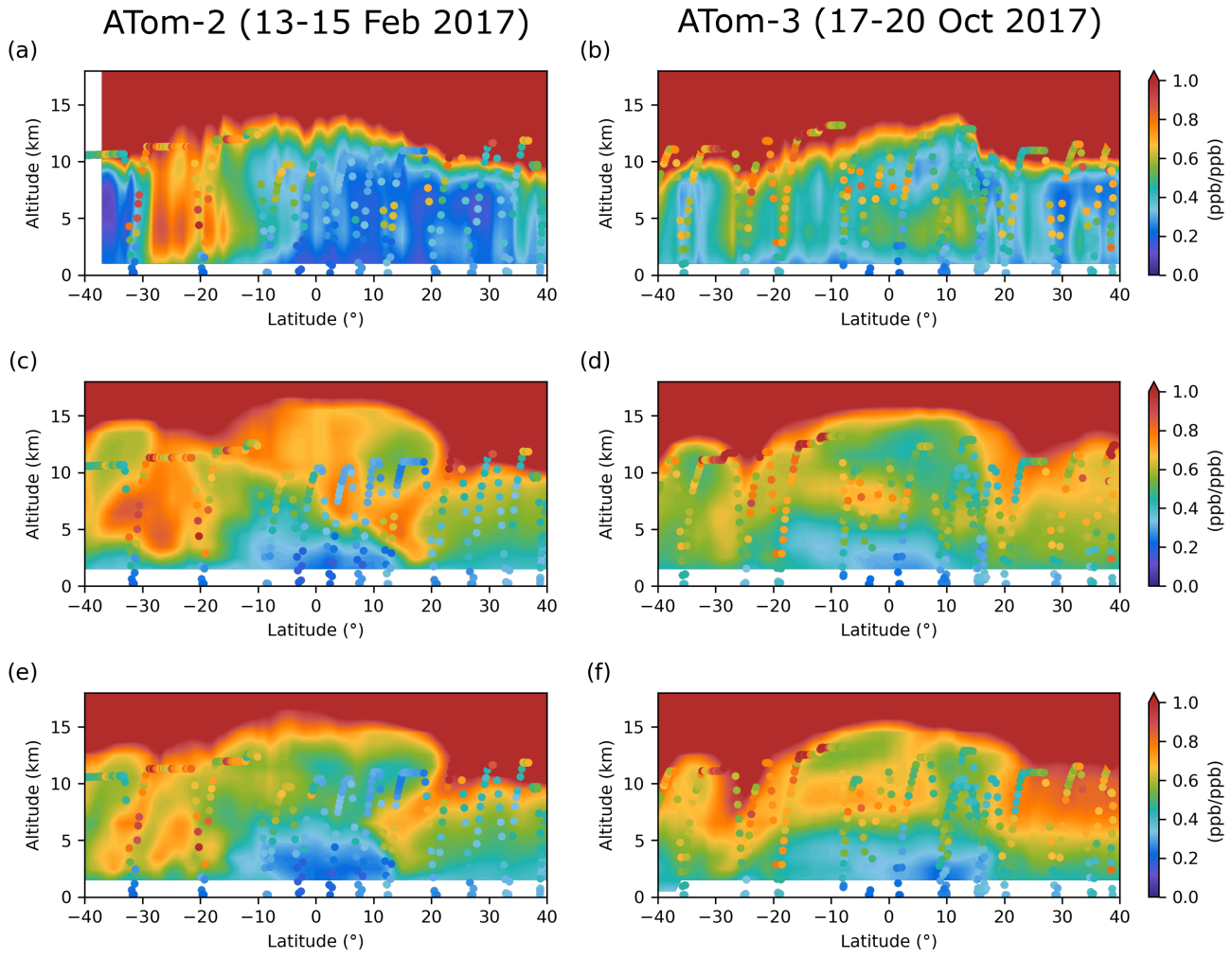

Figure 8: Vertical profiles of the ratio of ozone and CO concentrations averaged over the period from 13 to 15 February and from 17 to 20 October 2017. Dots indicate ATom-2 and Atom-3 observations. The ratios of (a) IASI+GOME2 and IASI, (b) TCR-2 and

(c) CAMS reanalysis are calculated by the average ozone and CO concentrations for the period from 13 to 15 February 2017 and from 17 to 20 October 2017, respectively, and are extracted along the ATom flight tracks.

The enhancement of the O_3/CO ratio over the South Atlantic (25° S) is also present in the two reanalyses. On the other hand, the two reanalyses display a second maximum around 20° N (Fig. 8d and e), which is not depicted by any of the observational datasets (satellite or in situ). This is collocated with a descending branch of a Hadley cell (see Sect. 3.4.3). Some punctual high values of the O_3/CO ratio measured by ATom-2 suggest the occurrence of a relatively small stratospheric instruction, contributing with ozone for air masses poor in CO concentrations. The reanalyses clearly overestimate the O_3/CO ratio in this area, likely linked to an overestimation of the magnitude and size of the stratospheric air intrusion (which is not observed by IASI+GOME2) combined with underestimations of CO concentrations by the reanalyses (Fig. 7c and e).

The ratio of IASI+GOME2 ozone and IASI CO generally shows less agreement with that of ATom-3 all along the track compared to the case of ATom-3 (Fig. 8a–b). The satellite retrievals generally show higher ratios except for a part of area in the Northern Hemisphere (10° N–20° N), likely linked to an underestimation of ozone concentrations. On the other hand, reanalyses clearly overestimate the O_3/CO ratio in this area.

3.4 Origins of ozone and CO reaching the Atlantic

Figure 9a shows a classification of multiple air masses (stratospheric air, marine air, urban air, biomass burning air, mixed pollution air, and well-mixed and aged air) during ATom-2 based on the method of Bourgeois et al. (2021). Here, well-mixed and aged air is defined as air mass with simultaneous low levels of biomass burning (HCN) and urban (C_2Cl_4) tracers. The other significant sources of CO (e.g., biogenic emissions and methane oxidation) and ozone precursors (e.g., lightning and soil emissions for NO_X, biogenic emission of VOCs) are included in the well-mixed and aged air mass category. This classification provides a very interesting picture of the complexity of the multiple contributions of the air masses along the transect. We clearly depict a strong urban influence north of 10° N between 2 and 10 km of altitude, a sector with rather weak ozone abundance and low O_3-to-CO ratio according to satellite/in situ measurements (Fig. 6a and 8a). Biomass burning emissions notably affect the low-to-upper troposphere (from 2 to 11 km of altitude) roughly between 25° S to 5° N, which are collocated with moderate and large abundances respectively ozone and CO (Fig. 7a) much likely associated with emissions from Central African fires. Marine and stratospheric influences can be seen along the transect near the ocean (below 2 km of altitude) and close to the tropopause (above 10 km of altitude, specifically near 20° S and 25° N), respectively.

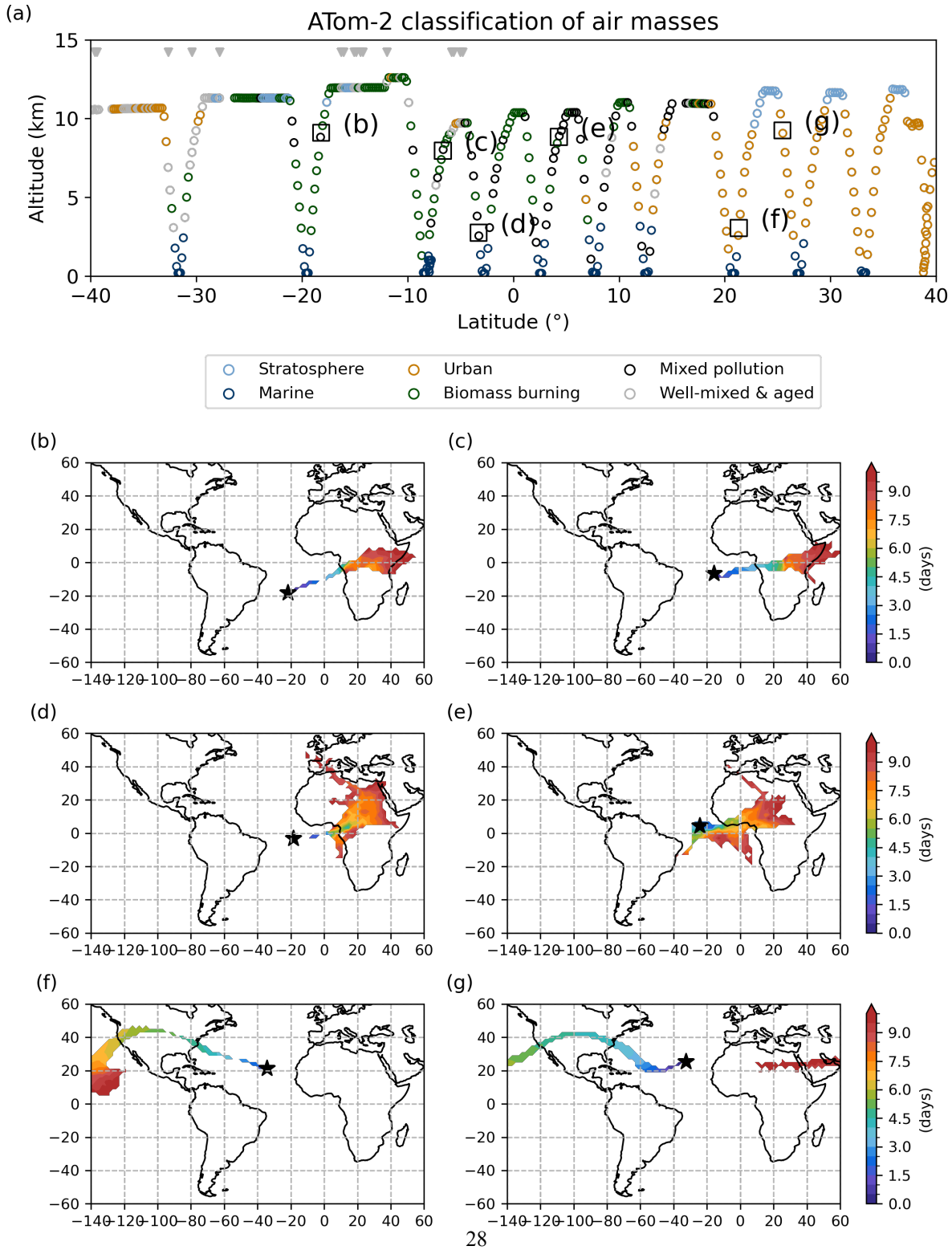
(a)
ATom-2 classification of air masses
Altitude (km)
Latitude (°)
(b)
(c)
(d)
(e)
(f)
(g)
Stratosphere
Marine
Urban
Biomass burning
Mixed pollution
Well-mixed & aged
(days)

Figure 9: Classification and origin of air masses along the transect sampled by ATom-2. (a) Air masses are classified into six categories: marine (navy), stratosphere (light blue), urban (light brown), biomass burning (dark green), mixed pollution (black), and well-mixed and aged air (grey). Grey triangles indicate the well mixed and aged air influenced by lightning emissions. (b–g) Colours indicate average time since trajectories are initialized with NCEP winds.

The influence of lightning in October is clearly less than that in February (Fig. 10a). We clearly depict a strong biomass burning influence in the south of 10° N and strong urban influence in the north of 20° N in the troposphere. The region between 10° N and 20° N seems to be a transition region where the air masses are classified into urban, biomass burning or well-mixed and aged air mass. Marine and stratospheric influences can be seen along the transect near the ocean (below 2 km of altitude) and close to the tropopause (above 10 km of altitude in the Southern Hemisphere), respectively. Biomass burning emissions notably affect the low-to-upper troposphere (from 2 to 11 km of altitude) roughly between 40° S to 10° N.

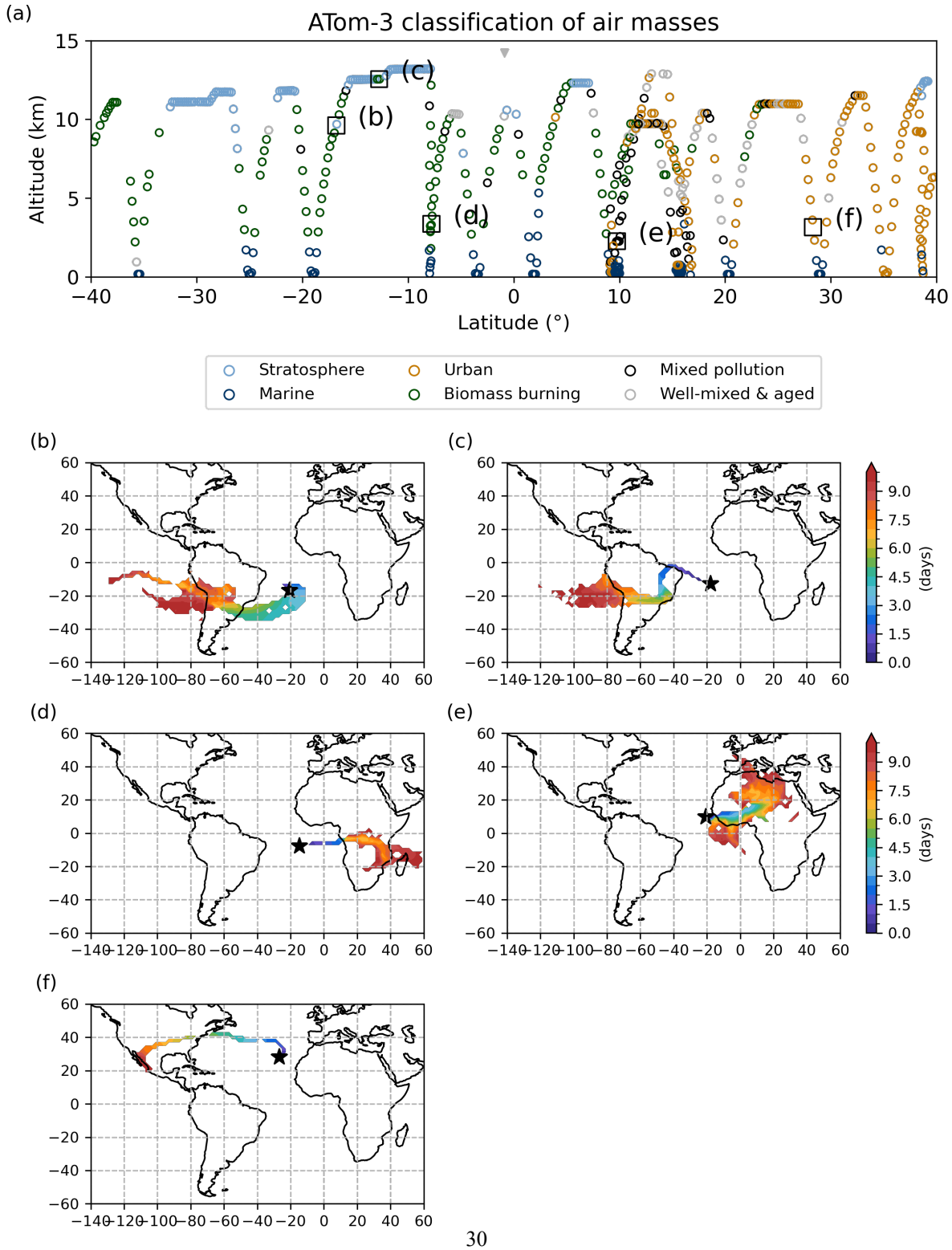
(a)
ATom-3 classification of air masses
Altitude (km)
Latitude (°)
(b)
(c)
(d)
(e)
(f)
Stratosphere
Marine
Urban
Biomass burning
Mixed pollution
Well-mixed & aged
(days)

Figure 10: Classification and origin of air masses along the transect sampled by ATom-3. (a) Air masses are classified into six categories: marine (navy), stratosphere (light blue), urban (light brown), biomass burning (dark green), mixed pollution (black), and well-mixed and aged air (grey). Grey triangles indicate the well mixed and aged air influenced by lightning emissions. (b–f) Colours indicate average time since trajectories are initialized with NCEP winds.

To further analyse the chemical composition and origin of the air masses sampled along the ATom-2 transect, we illustrate the correlative variation of NO_X and HCN (the biomass burning tracer) concentrations measured by the aircraft (Fig. 11a). Marine, urban, and mixed pollution air masses generally show low NO_X concentrations. Stratosphere, biomass burning, and well-mixed and aged air masses show higher NO_X concentrations. There are two possible sources of NO_X in well-mixed and aged air: boundary layer (including biogenic and soil emissions) and upper troposphere (lightning emission). To distinguish these two sources, we use probability of boundary layer influences (percentage of time the air masses are located within the boundary layer) determined by 30-day back trajectories provided by the ORNL DAAC (Ray, 2021; Fig. 11b). We define air masses influenced by lightning as those with high NO_X concentration (larger than the regional median of 0.033 ppb for ATom-2 and 0.054 ppb for ATom-3) and low probability of boundary layer influences (lower than 50 %). The significant influence of lightning is indicated by grey triangles in Fig. 9a. Well-mixed and aged air masses with relatively high NO_X concentration in Fig. 11a show low probability of boundary layer influence or origin. Therefore, these air masses might be influenced by lightning emissions.

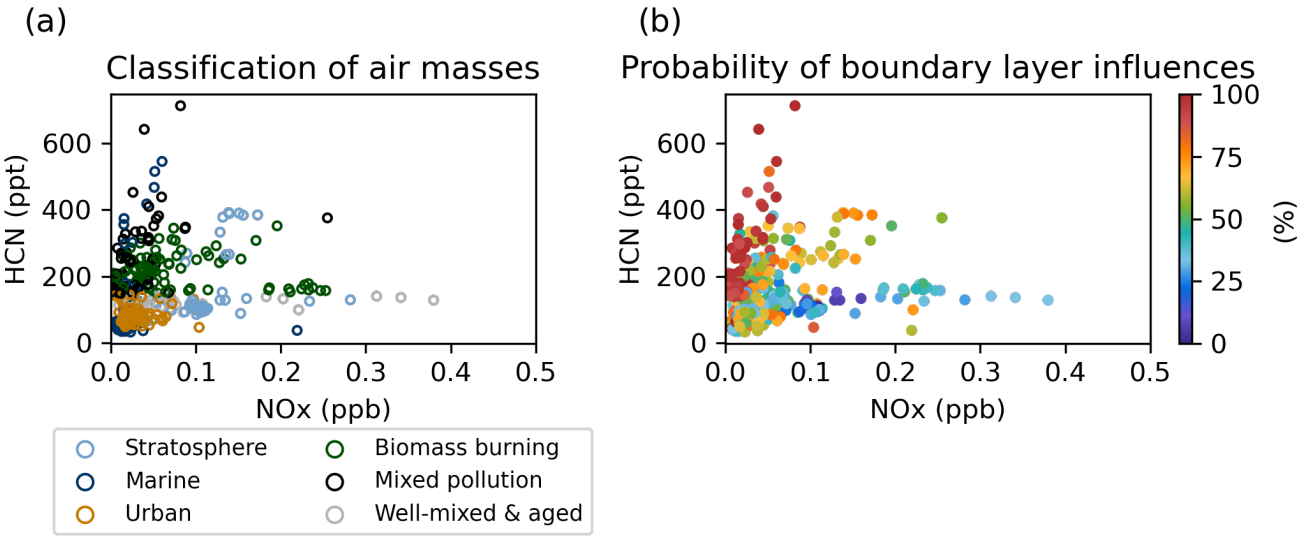

Figure 11: Scatterplots of NO_X vs. HCN (biomass burning tracer) of ATom-2 observation with colours indicating (a) the air masses classification into six categories: marine (navy), stratosphere (light blue), urban (light brown), biomass burning (dark green), mixed pollution (black), well-mixed and aged air (grey), and (b) the probability of boundary layer influences.

The capability to identify the origin and nature of air masses by the satellite observations is illustrated in Fig. 12a is terms of the relationship of the abundance of CO and ozone, coloured according to their origin (derived from ATom-2 measurements). We remark a rather similar distribution of values as obtained for the scatter of values of HCN vs NOx in Fig. 11a. Urban-influenced air masses (light brown circles in Fig. 12a) are mostly associated with moderate abundances of both CO and ozone (up to respectively 150 and 60 ppb). Larger concentrations of ozone (> 70 ppb) retrieved by satellite correspond to stratospheric air masses around 40°N. Some of these samples identified as influenced by the stratosphere and some as urban (as the air masses below, maybe due to a coarser vertical resolution of the satellite retrieval). CO-rich air masses correspond to those influenced by biomass burning, mixed-pollution and marine (with CO mixing down near the ocean surface). Whereas these features are clearly depicted by the satellite retrievals, they are not clearly modelled by the reanalyses (Fig. 12c). This is illustrated in Fig. 12c for TCR-2 that show less clear patterns distinguishing the chemical composition air masses. Very similar results are obtained for CAMS reanalysis (Fig. S5).

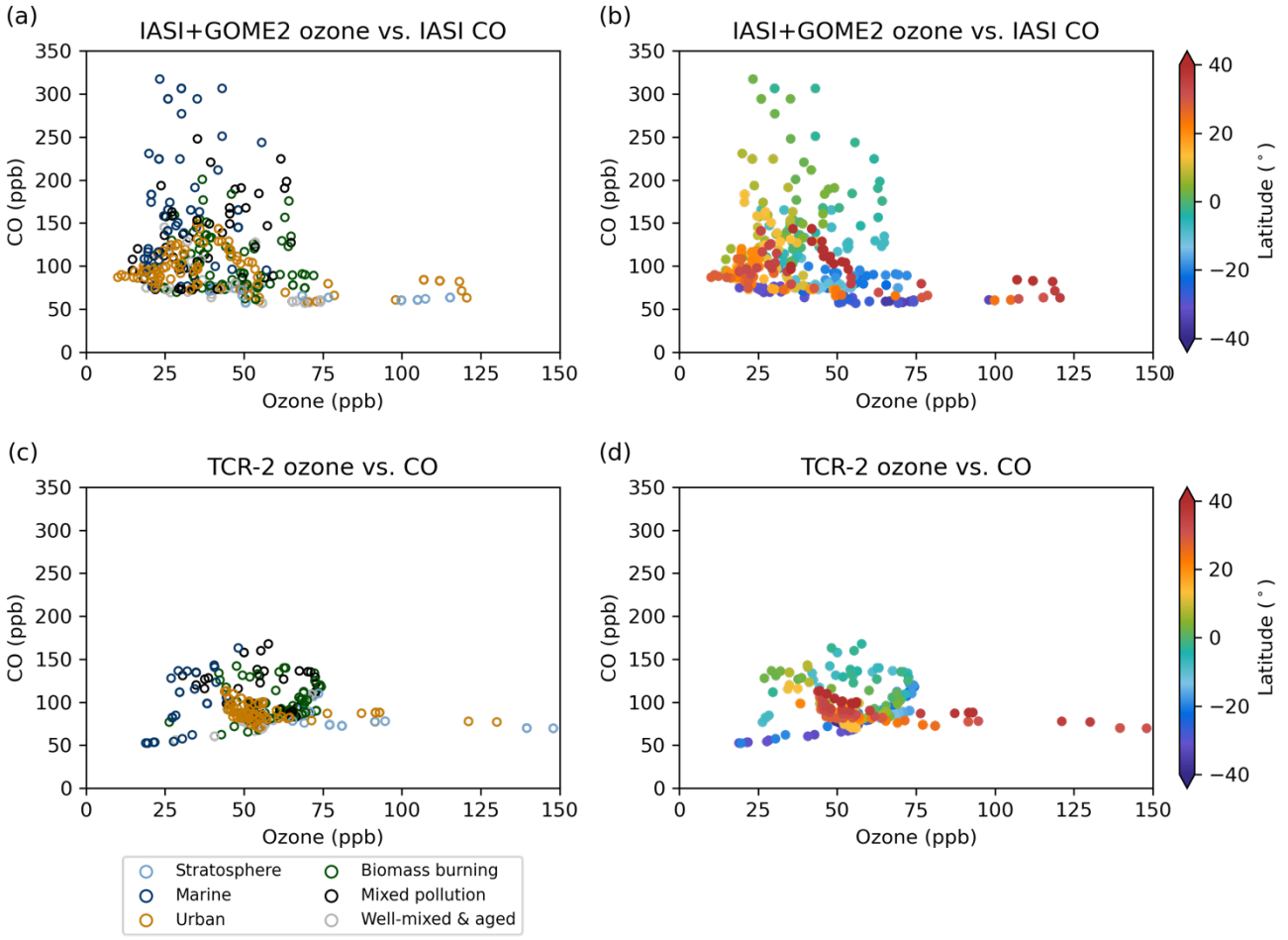

Figure 12. Scatterplots of CO vs. ozone for air masses sampled by ATom-2 derived from (a and b) satellite measurements of respectively IASI and IASI+GOME2 and (c and d) TCR-2. Colours indicate (a and c) the air masses classification into six categories (idem as Figs. 9a and 10a) and (b and d) the latitude location.

The following subsections use the categorization in Fig. 9a and 10a to describe the origin of air masses in the Tropical (Sect. 3.4.1), Southern (Sect. 3.4.2) and Northern (Sect. 3.4.3) Atlantic.

3.4.1 The Tropical Atlantic

As shown in Sect. 3.3, large CO enhancement is observed around the equator in three satellite and reanalysis products and ATom-2 observation (the left panels of Fig. 7). Chemical tracers suggest that most of these air masses rich in CO are classified into marine air, biomass burning air or mixed pollution air (Fig. 9a). Back trajectory analyses indicate that these CO-enriched

air masses in the lower troposphere (15° S–15° N) passed over the Gulf of Guinea, Western, Central and Northern Africa (Figs. 9d). In February, biomass burning is active in Western (south of the Sahara) and Central Africa (Fig. 1c). These results indicate that the biomass burning emissions with rich-CO are transported from the southern part of Western Africa and Central Africa to the remote Tropical Atlantic via the Gulf of Guinea by southeasterly winds. On the other hand, ozone concentration in the lower troposphere around the equator is moderate according to the three products and ATom-2 observations (the left panels of Fig. 6). Ozone enhancements are remarked in the Gulf of Guinea and the coastal countries (the left panels of Fig. 4), while it takes over 6 days for the air masses to travel from the coast to the ATom-2 track far in the Atlantic (Fig. 9d). In this location, the ozone attributed to biomass burning emissions is approximately 4 ppb (~10 %) from the surface to 5 km between 15° S and 15° N, according to an estimation of the ozone attributed to biomass burning emissions using biomass burning tracer (Fig. 13a). This is consistent with significant sinks of ozone often encountered within a lower tropical marine troposphere. In these conditions, the photochemical lifetime of ozone is typically reduced to a few days because of abundant actinic radiation, ample water vapor, and negligible NO_X. (e.g., Crutzen et al., 1999). The high abundance of water vapor in the equatorial region is confirmed by ERA5 reanalyses (Fig. S6e).

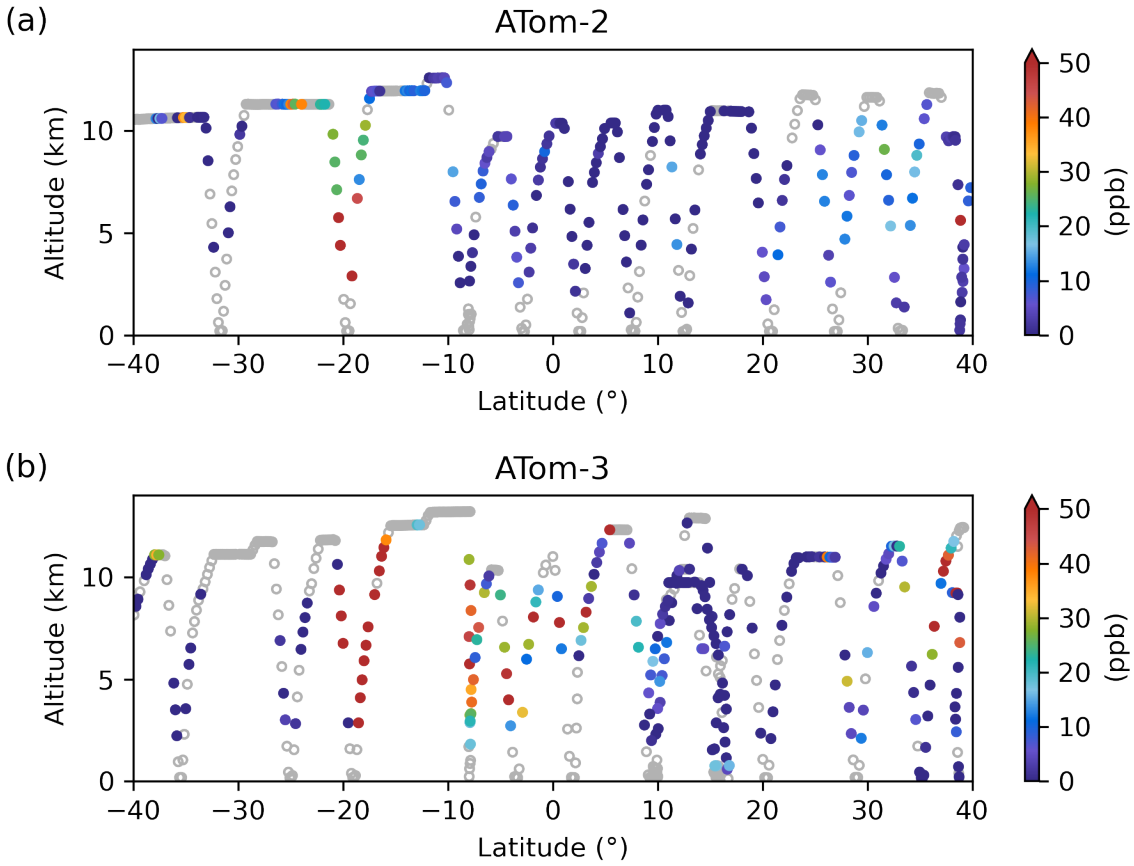

Figure 13: Vertical profile of ozone concentration attributed to biomass burning during (a) Atom-2 and (b) Atom-3. We consider here air masses classified as mainly "biomass burning", "mixed pollution" and "urban", and grey for other categories.

635 Strong upward motion can be observed around the equator (Fig. S6c). High relative humidity can also be observed in the middle and upper troposphere as well as in the lower troposphere around the equator (Fig. S6e). These results indicate that the air in the marine boundary layer is uplifted to the upper troposphere by the deep convection, as indicated by collocated OLR below 220 W m^{-2} (Fig. 1a). Strong downward motion can be observed between 20° N and 30° N (Fig. S6c). It is indicating a descending branch of a Hadley cell.

640 Another CO plume collocated with high relative humidity can be identified in the upper troposphere (> 9 km) between 10° S and 20° N (the left panels of Fig. 7 and Fig. S6e), although not clearly by IASI CO. Most of these CO-rich air masses are classified into biomass burning air, mixed pollution air or well-mixed and aged air (Fig. 9a). Back trajectory analysis indicates that most of the air masses are transported from Western and Central Africa to the remote Atlantic via the Gulf of Guinea (Figs. 9e). Some well-mixed and aged air masses show high NO_X concentration and low probability of boundary layer

influence (Fig. 9a). This may correspond to the presence of lightning-produced NO_X, impacting ozone concentrations. These results suggest that deep convection occurs around the equator, likely injecting water vapor and CO into the upper troposphere from the lower troposphere. The ozone attributed to biomass burning emissions is approximately 2 ppb (~4%) over 9 km between 10°S and 20°N.

As shown in Sect. 3.3, large CO enhancement is observed between 25 °S and the equator in three satellite and reanalysis products and ATom-3 observation (the right panels of Fig. 7). This CO plume locates between 3–7 km of altitude in two reanalysis products. In addition, CAMS reanalysis and ATom-3 show another CO plume between 12–17 km. Chemical tracers suggest that most of tropospheric air masses in the Southern Hemisphere are classified into marine air or biomass burning air (Fig. 10a). IASI+GOME2 shows an enhancement of ozone below 6 km of altitude, whereas two reanalysis products show an enhancement of ozone over 5 km. ATom-3 shows higher ozone concentrations than three satellite and reanalysis products between 20° S and 0° in the troposphere (the right panels of Fig. 6). The relative humidity profile from ERA5 indicates that the sources of air masses between 2–6 km, 6–12 km and 12–17 km of altitude are different: the bottom air with moderate relative humidity (> 50 %), the middle air with low relative humidity (< 30 %) and the upper air with high relative humidity (> 60 %) (Fig. S7e). Back trajectory analyses indicate that the air masses in the lower troposphere passed over the Congo Basin and Southern Africa by easterly winds (the right panels of Fig. 4 and Fig. 10d), and that the air masses in the middle and upper troposphere passed over Brazil and south of Brazil by northwesterly winds (the right panels of Fig. 5 and Fig. 10b–c). In October, biomass burning is active in the Congo Basin, Southern Africa and South America (Fig. 1d). The ozone attributed to biomass burning emissions is approximately 22 ppb (~31 %) from the surface to 15 km between 20° S and the equator, according to an estimation of the ozone attributed to biomass burning emissions using biomass burning tracer (Fig. 13b). These results indicate that the biomass burning emissions from both continents are transported and the make a triple layered structure over the Tropical Atlantic. The influence of urban emissions increases between 10° N and 20° N (Fig. 10a). ATom-3 and two reanalyses show very low ozone concentrations in this region (the right panels of Fig. 6). Back trajectory analyses indicate that the air masses passed over Western Africa and the Saharan Desert (Fig. 10f).

3.4.2 The Southern Atlantic

At around 20° S in the upper troposphere, three satellite/reanalysis ozone products and ATom-2 in situ observations clearly depict a stratospheric intrusion (the left panels of Fig. 6). Very low potential vorticity (< –2 PVU) and downward motion from ERA5 also indicate downward transport of air masses from the upper troposphere and the lower stratosphere at around 20° S (Fig. S6a and c). The ozone plume extends from the upper troposphere at 20° S to the middle troposphere at the equator according to the reanalyses. Concomitant relative humidity with respect to the ozone plume is low (Fig. S6e), which is typical for stratospheric air. However, this ozone plume is also collocated with a moderate CO plume (the left panels of Fig. 7), which is not expected for pure stratospheric air. According to the classification shown in Fig. 9a, most of air masses within this plume

correspond to stratosphere air, biomass burning air, well-mixed and aged air, or mixed pollution air. The ozone attributed to biomass burning emissions is approximately 12 ppb (~17 %) over 7 km between 25° S and 5° N and approximately 24 ppb (~29 %) over 3 km between 25° S and 15° S (Fig. 13a). Back trajectory analysis indicates that the air is from Central and Eastern Africa (Fig. 9b–c). These results suggest that the ozone plume is influenced by both stratospheric exchanges and biomass burning emissions. Some well-mixed and aged air masses show high NO_X concentration and low probability of boundary layer influence (Fig. 9a). According to the discussion in Fig. 11, these conditions suggest the influence of lightning-produced NO_X as ozone precursor. Back trajectories confirm that these lightning-influenced air masses originate from a lightning active region in South America (Fig. 1a).

3.4.3 The Northern Atlantic

The two reanalyses show a stratospheric intrusion in the UTLS around 25° N, co-located with a descending branch of the Hadley cell, whereas IASI+GOME2 does not show such a feature (the left panels of Fig. 6) and ATom-2 in a lower clearly lower magnitude (see discussions in Sect. 3.2). In this region, we remark high potential vorticity, low relative humidity (Fig. S6a and e) and strong subsidence at altitudes between 6 and 10 km (Fig. S6c). The downward motion speed derived from ERA5 reanalyses is greater than 1 cm s^{-1} in absolute terms, which is significantly larger than the typical value for tropical clear-sky regions (Gettelman et al., 2004; Das et al., 2016). The CO concentrations collocated with the ozone plume are low (the left panels of Fig. 8). Although the origin of these air masses is clearly identified, the magnitude of downward transport of ozone from the stratosphere is likely overestimated by the reanalyses.

Below the UTLS around 20–25° N, back trajectories from the lower and upper troposphere indicate that the air masses originate from North America (Fig. 9f–g). Most of the air mass is classified to urban air in the Northern Hemisphere, especially over 20° N (Fig. 9a). The influence of biomass burning is seen closer to the equator. These results suggest that the reanalyses likely overestimate the urban influence of the Northern Hemisphere over the Atlantic.

The two reanalyses show a stratospheric intrusion in the UTLS around 25° N, co-located with a descending branch of the Hadley cell, whereas IASI+GOME2 and ATom-3 do not show such a feature (the right panels of Fig. 7). In this region, we remark high potential vorticity and strong subsidence at altitudes between 8 and 15 km (Fig. S7a and c). However, relative humidity is high (Fig. S7e), which is not typical feature of stratospheric air. It suggests that the magnitude of downward transport of ozone from the stratosphere is likely overestimated by the reanalyses. Most of the air mass is classified to urban air in the Northern Hemisphere, especially over 20° N (Fig. 10a). The influence of biomass burning is seen closer to the equator. Back trajectories from the lower troposphere indicate that the air masses originate from North America (Fig. 10g).

4 Conclusions

We have presented an analysis of the tropospheric ozone spatial distribution and its origins using satellite (IASI+GOME2), in situ observations (ATom-2 and ATom-3) and two global reanalyses (TCR-2 and CAMS reanalysis) over the Tropical and South Atlantic in February and October 2017. Seasonal variation of regional discrepancies (expressed as spatial coefficient of variations) between the satellite observations and the reanalyses of monthly ozone distribution over the Tropical Atlantic (25° S–25° N, 34° W–18° W) show a clear seasonality corresponding to two biomass burning seasons and two transition seasons in Africa. The largest CV among these datasets are seen for the months of January and February. In this last period, the region is likely influenced by biomass burning emissions form the southern part of West Africa and Central Africa and deep convection over the Gulf of Guinea (over the Ocean), Central and Southern Africa (as depicted by the frequent lightning activity). On the contrary, the highest average ozone and small CV can be seen in October, corresponding to the biomass season in the Southern Hemisphere. Comparisons of horizontal distributions of monthly ozone in the lowermost troposphere (surface–3 km) in February 2017 show that IASI+GOME2, TCR-2 and CAMS reanalysis datasets display high concentration of ozone from Western Africa to the Gulf of Guinea. Only IASI+GOME2 depicts an enhancement of lowermost tropospheric ozone north of the St. Helena anticyclone. In the middle and upper troposphere, all products show a horseshoe-shaped structure of high concentration of ozone from Southern and Western Africa to the east of Brazil. IASI+GOME2 show lower ozone concentration in the South America compared to two chemistry reanalysis products. In October 2017, all products show high concentrations of ozone in the Congo Basin, Brazil and the outflow over the South Atlantic in the lowermost troposphere. We can also see moderate enhancement of ozone in south of the Sahara Desert. In these regions, In the middle and upper troposphere, all products show high concentrations of ozone in the Congo Basin, Brazil and the outflow over the South Atlantic. The tropospheric ozone spatial distributions are generally similar for the monthly means in February and October 2017 and the average in the 3-day and 4-day periods when ATom-2 and ATom-3 in situ measurements are available (13–15 February and 17–20 October 2017). We analyse these vertical profiles along a south-north track from 40° S to 40° N to assess the capability of satellite and chemistry reanalysis products to characterize the spatial distribution of the tropospheric ozone over the Tropical Atlantic. We clearly observe that only the IASI+GOME2 satellite approach is able to describe the strong gradient of significant tropospheric ozone enhancements in the Southern Hemisphere and low abundances in the Northern Hemisphere, in agreement with ATom-2 in situ measurements. An enhancement of ozone in the north of the St. Helena anticyclone between 10° S and 20° S is consistently observed by both IASI+GOME2 and ATom-2, whereas the two reanalyses show low ozone values below 20 ppb. North of the equator, all two reanalyses particularly fail to depict the weak ozone concentrations consistently observed by satellite and in situ sensors (IASI+GOME2 and ATom-2 agree both in absolute values and correlation). This is partly explained by a significant ozone enhancement displayed by two chemistry reanalyses in the descending branch of the Hadley cell at around 25° N, which is not depicted by IASI+GOME2 nor ATom-2. Back trajectory analysis indicates that these air masses in the lower and upper troposphere originate from North America.

On the other hand, the reanalysis products reproduce the distribution of ozone relatively well during the ATom-3 period. IASI+GOME2 ozone concentrations are generally lower than those of ATom-3. The ozone distribution of two reanalysis products is characterized by an ozone plume in the troposphere between 25° S and the equator at 5–10 km of altitude. IASI+GOME2 depicts the ozone plume at 3–6 km, which is lower than the altitude of the plume shown by the reanalysis products. A moderate enhancement of ozone can be seen in the north of 10 °N. These enhancements of ozone concentration correspond to those seen in the lower troposphere horizontal distribution over the Atlantic. The horizontal distribution of ozone from the reanalyses presents lower concentrations in the lowermost troposphere around the equator. Particularly in the Northern Hemisphere (north of 15° N), we can observe large difference of ozone concentration between IASI+GOME2 and two reanalyses. This difference corresponds to concentrations 20 ppb lower for IASI+GOME2 than for the reanalyses. In addition, an enhancement of ozone from the upper troposphere to the middle and lower troposphere can be observed in reanalyses around 25° N.

Using ozone and CO abundances from satellite and in situ measurements, together with measurements of several tracers, we describe the sources of ozone and CO plumes over the tropical Atlantic. Around the equator, an CO plume with low-ozone is observed in the lowermost troposphere by all datasets (satellite observations, in situ measurements and two reanalyses) during 13–15 February 2017. Most of air masses is classified into marine air (near the ocean), biomass burning air or mixed pollution air and passed over the Gulf of Guinea, Western, Central and Northern Africa. Far from the coast (10° S, 15° W) in the ATom-2 flight track, the amount of ozone attributed to biomass burning emissions is low with the value of approximately 7 ppb (~27 %) from the surface to 5 km between 15° S and 15° N. This is likely link to active sinks of tropospheric ozone during the transport from the continent due to the high relative humidity. During 17–20 October, CO plume caused by biomass burning from the Congo Basin and Brazil and is located between 20° S and the equator. The ozone attributed to biomass burning emissions is approximately 22 ppb (~31 %) from the surface to 15 km between 20° S and the equator.

During ATom-2 period, strong upward motion around the equator injects water vapor and CO into the upper troposphere from the lower troposphere. Most of air masses within the CO plume in the upper troposphere (> 9 km) between 10° S and 20° N is classified as influenced by biomass burning, mixed pollution air or well-mixed and aged air. This CO plume is transported from Western and Central Africa to the remote Atlantic via the Gulf of Guinea. In addition, some well-mixed and aged air masses might be influenced by lightning-produced NO_X indicated by high NO_X concentration and low probability of boundary layer influence. The ozone attributed to biomass burning emissions is approximately 2 ppb (~4 %). At around 20 °S in the upper troposphere, all datasets show a stratospheric intrusion. An ozone plume with low-relative humidity and high-CO transported from Central and Eastern Africa is observed in the middle and upper troposphere. In this region, the ozone plume in the lower troposphere only depicted IASI+GOME2 and ATom-2 north of St. Helena anticyclone is classified as stratosphere air, biomass burning air, well-mixed and aged air, or mixed pollution air. The ozone attributed to biomass burning emissions is approximately 13 ppb (~17 %) over 7 km between 25° S and 5° N and approximately 38 ppb (~50 %) over 3 km between 25° S and 15° S. In addition, lightning-produced NO_X might also impact on the ozone concentration. Air masses in the Northern Hemisphere with weak concentrations of ozone (over 20° N) are classified as influenced by urban sources (from North America

according to back trajectories). These results suggest that the reanalyses overestimate the abundance of tropospheric ozone over the remote locations in the Tropical Atlantic for air masses influenced by urban sources of North America in February 2017.

During ATom-3 period, large CO enhancement is observed between 25 °S and the equator in three satellite and reanalysis products and ATom-3 observation. Our results indicate that the biomass burning emissions from both continents are transported and the make a triple layered structure over the Tropical Atlantic. The air masses in the lower troposphere passed over the Congo Basin and Southern Africa by easterly winds, and the air masses in the middle and upper troposphere passed over Brazil and south of Brazil by northwesterly winds. The two reanalyses show a stratospheric intrusion in the UTLS around 25° N, co-located with a descending branch of the Hadley cell, whereas IASI+GOME2 and ATom-3 do not show such a feature. In this region, we remark high potential vorticity and strong subsidence at altitudes between 8 and 15 km. However, relative humidity is high, which is not typical feature of stratospheric air. It suggests that the magnitude of downward transport of ozone from the stratosphere is likely overestimated by the reanalyses. Most of the air mass is classified to urban air in the Northern Hemisphere, especially over 20° N. Back trajectories from the lower troposphere indicate that the air masses originate from North America.

Data availability

The IASI+GOME2 ozone and the IASI CO datasets derived from MetOp-B global measurements are available on the French data centre AERIS (https://iasi.aeris-data.fr/).

The TCR-2 dataset is available at https://tes.jpl.nasa.gov/tes/chemical-reanalysis/

The CAMS reanalysis dataset has been downloaded at the Atmosphere Data Store (ADS) (https://ads.atmosphere.copernicus.eu/).

The ATom data are distributed by the Oak Ridge National Laboratory Distributed Active Archive Center (ORNL DAAC) (https://daac.ornl.gov/).

ERA5 data have been downloaded from the Climate Data Store (https://cds.climate.copernicus.eu/).

The WWLLN Global Lightning Climatology (WGLC) global gridded lighting timeseries is available at https://github.com/ARVE-Research/WGLC.

The monthly OLR data is distributed by the National Oceanic and Atmospheric Administration (NOAA) Physical Science Laboratory (PSL) (https://psl.noaa.gov/).

The active fire products (MCD14ML Collection 6) is distributed by the Fire Information for Resources Management System (FIRMS) (https://firms.modaps.eosdis.nasa.gov/).

Author contributions

SO and JC conducted the research work and lead the writing of the main manuscript. JC provided the IASI+GOME2 satellite data. CB provided support in the production of IASI+GOME2 data. KM provided the TCR-2 tropospheric chemistry reanalysis data. All authors (SO, JC…) contributed to the discussions, refinement of the results and improvements of the paper.

Competing interests

The contact author has declared that none of the authors has any competing interests.

Acknowledgements

Authors acknowledge the financial support of the Centre National des Etudes Spatiales (CNES, the French Space Agency) via the SURVEYPOLLUTION and TOTICE research projects from the TOSCA (Terre Ocean Surface Continentale Atmosphère) committee, the Université Paris Est Créteil (UPEC), and the Centre National des Recherches Scientifiques–Institut National des Sciences de l'Univers (CNRS-INSU), for helping in achieving this research work and its publication.We also acknowledge the AERIS data centre for providing IASI+GOME2 ozone and IASI CO (developed by the Université Libre de Bruxelles and the LATMOS laboratory) datasets, the ADS for providing CAMS reanalysis dataset, the CDS for providing ERA5 datasets, the ORNL DAAC for providing the ATom datasets, the WWLLN providing the WGLC lightning timeseries, NOAA/PSL for providing the OLR data, and the FIRMS for providing the active fire products. We also acknowledge the support of the NASA Atmospheric Composition: Aura Science Team Program (19-AURAST19-0044), Earth Science U.S. Participating Investigator program (22-EUSPI22-0005), ACMAP (22-ACMAP22-0013), and the NASA TROPESS project. Part of this work was conducted at the Jet Propulsion Laboratory, California Institute of Technology, under contract with NASA. Ilann Bourgeois is also acknowledged for providing the method of tracers.

References

Andela, N. and van der Werf, G. R.: Recent trends in African fires driven by cropland expansion and El Niño to La Niña transition, Nature Clim. Change, 4, 791–795, https://doi.org/10.1038/NCLIMATE2313, 2014.

Andreae, M. O.: Emission of trace gases and aerosols from biomass burning – an updated assessment, Atmos. Chem. Phys., 19, 8523–8546, https://doi.org/10.5194/acp-19-8523-2019, 2019.

Atkinson, R.: Atmospheric chemistry of VOCs and NO_x, Atmos. Environ., 34, 2063–2101, https://doi.org/10.1016/S1352-2310(99)00460-4, 2000.

Bourgeois, I., Peischl, J., Neuman, J. A., Brown, S. S., Thompson, C. R., Aikin, K. C., Allen, H. M., Angot, H., Apel, E. C., Baublitz, C. B., Brewer, J. F., Campuzano-Jost, P., Commane, R., Crounse, J. D., Daube, B. C., DiGangi, J. P., Diskin, G. S., Emmons, L. K., Fiore, A. M., Gkatzelis, G. I., Hills, A., Hornbrook, R. S., Huey, L. G., Jimenez, J. L., Kim, M., Lacey,

F., McKain, K., Murray, L. T., Nault, B. A., Parrish, D. D., Ray, E., Sweeney, C., Tanner, D., Wofsy, S. C. and Ryerson, T. B.: Large contribution of biomass burning emissions to ozone throughout the global remote troposphere, Proc. Natl. Acad. Sci., 118, e2109628118, https://doi.org/10.1073/pnas.2109628118, 2021.

Cai, Z., Liu, Y., Liu, X., Chance, K., Nowlan, C. R., Lang, R., Munro, R. and Suleiman, R.: Characterization and correction of Global Ozone Monitoring Experiment 2 ultraviolet measurements and application to ozone profile retrievals, J. Geophys. Res., 117, D07305, https://doi.org/10.1029/2011JD017096, 2012.

Cecil, D. J., Buechler, D. E. and Blakeslee, R. J.: Gridded lightning climatology from TRMM-LIS and OTD: Dataset description, Atmos. Sci., 135, 404–414, https://doi.org/10.1016/j.atmosres.2012.06.028, 2014.

Colombi, N., Miyazaki, K., Bowman, K. W., Neu, J. L. and Jacob, D. J.: A new methodology for inferring surface ozone from multispectral satellite measurements, Environ. Res. Lett., 16, 105005, doi:10.1088/1748-9326/ac243d, 2021.

Crutzen, P. J., Lawrence, M. G. and Pöschl, U.: On the background photochemistry of tropospheric ozone, Tellus B Chem. Phys. Meteorol., 51, 123, https://doi.org/10.3402/tellusb.v51i1.16264, 1999.

Cuesta, J., Costantino, L., Beekmann, M., Siour, G., Menut, L., Bessagnet, B., Landi, T. C., Dufour, G., and Eremenko, M.: Ozone pollution during the COVID-19 lockdown in the spring of 2020 over Europe, analysed from satellite observations, in situ measurements, and models, Atmos. Chem. Phys., 22, 4471–4489, https://doi.org/10.5194/acp-22-4471-2022, 2022.

Cuesta, J., Eremenko, M., Liu, X., Dufour, G., Cai, Z., Höpfner, M., von Clarmann, T., Sellitto, P., Foret, G., Gaubert, B., Beekmann, M., Orphal, J., Chance, K., Spurr, R. and Flaud, J.-M.: Satellite observation of lowermost tropospheric ozone by multispectral synergism of IASI thermal infrared and GOME-2 ultraviolet measurements over Europe, Atmos. Chem. Phys., 13, 9675–9693, https://doi.org/10.5194/acp-13-9675-2013, 2013.

Cuesta, J., Kanaya, Y., Takigawa, M., Dufour, G., Eremenko, M., Foret, G., Miyazaki, K. and Beekmann, M.: Transboundary ozone pollution across East Asia: Daily evolution and photochemical production analysed by IASI+GOME2 multispectral satellite observations and models, Atmos. Chem. Phys., 18, 9499–9525, doi:10.5194/acp-18-9499-2018, 2018.

Das, S. S., Ratnam, M. V., Uma, K. N., Subrahmanyam, K. V., Girach, I. A., Patra, A. K., Aneesh, S., Suneeth, K. V., Kumar, K. K., Kesarkar, A. P., Sijikumar, S., and Ramkumar, G.: Influence of tropical cyclones on tropospheric ozone: possible implications, Atmos. Chem. Phys., 16, 4837–4847, https://doi.org/10.5194/acp-16-4837-2016, 2016.

Dee, D. P., Uppala, S. M., Simmons, A. J., Berrisford, P., Poli, P., Kobayashi, S., Andrae, U., Balmaseda, M. A., Balsamo, G., Bauer, P., Bechtold, P., Beljaars, A. C. M., van de Berg, L., Bidlot, J., Bormann, N., Delsol, C., Dragani, R., Fuentes, M., Geer, A. J., Haimberger, L., Healy, S. B., Hersbach, H., Hólm, E. V., Isaksen, L., Kållberg, P., Köhler, M., Matricardi, M., Mcnally, A. P., Monge-Sanz, B. M., Morcrette, J.-J., Park, B.-K., Peubey, C., de Rosnay, P., Tavolato, C., Thépaut, J.-N. and Vitart, F.: The ERA-Interim reanalysis: configuration and performance of the data assimilation system, Q. J. R. Meteorol. Soc., 137, 553–597, https://doi.org/10.1002/qj.828, 2011.

Dowden, R. L., Brundell, J. B. and Rodger, C. J.: VHF lightning location by time of group arrival (TOGA) at multiple site, J. Atmos. Sol.-Terr. Phys., 64, 817–830, https://doi.org/10.1016/S1364-6826(02)00085-8, 2002.

Dufour, G., Eremenko, M., Griesfeller, A., Barret, B., Leflochmoën, E., Clerbaux, C., Hadji-Lazaro, J., Coheur, P. F. and Hurtmans, D.: Validation of three different scientific ozone products retrieved from IASI spectra using ozonesondes, Atmos. Meas. Tech., 5, 611–630, https://doi.org/10.5194/amt-5-611-2012, 2012.

Elshorbany, Y., Ziemke, J. R., Strode, S., Petetin, H., Miyazaki, K., De Smedt, I., Pickering, K., Seguel, R. J., Worden, H., Emmerichs, T., Taraborrelli, D., Cazorla, M., Fadnavis, S., Buchholz, R. R., Gaubert, B., Rojas, N. Y., Nogueira, T., Salameh, T., and Huang, M.: Tropospheric ozone precursors: global and regional distributions, trends, and variability, Atmos. Chem. Phys., 24, 12225–12257, https://doi.org/10.5194/acp-24-12225-2024, 2024.

Eremenko, M., Dufour, G., Foret, G., Keim, C., Orphal, J., Beekmann, M., Bergametti, G. and Flaud, J.-M.: Tropospheric ozone distributions over Europe during the heat wave in July 2007 observed from infrared nadir spectra recorded by IASI, Geophys. Res. Lett., 35, L18805, https://doi.org/10.1029/2008GL034803, 2008.

Falk, S., Vollsnes, A. V., Eriksen, A. B., Stordal, F. and Berntsen, T. K.: Technical note: Quality assessment of ozone reanalysis products and gap-filling over subarctic Europe for vegetation risk mapping, Atmos. Chem. Phys., 21, 15647–15661, https://doi.org/10.5194/acp-21-15647-2021, 2021.

Fishman, J., J., Hoell Jr., M., Bendura, R. D., McNeal, R. J. and Kirchhoff, V. W. J. H.: NASA GTE TRACE A experiment (September–October 1992): Overview, J. Geophys. Res., 101, 23865–23879, https://doi.org/10.1029/96JD00123, 1996.

Fishman, J. and Larsen, J. C.: Distribution of total ozone and stratospheric ozone in the tropics: Implications for the distribution of tropospheric ozone, J. Geophys. Res., 92, 6627–6634, https://doi.org/10.1029/JD092iD06p06627, 1987.

Flemming, J., Huijnen, V., Arteta, J., Bechtold, P., Beljaars, A., Blechschmidt, A. M., Diamantakis, M., Engelen, R. J., Gaudel, A., Inness, A., Jones, L., Josse, B., Katragkou, E., Marecal, V., Peuch, V.-H., Richter, A., Schultz, M. G., Stein, O. and Tsikerdekis, A.: Tropospheric chemistry in the Integrated Forecasting System of ECMWF, Geosci. Model Dev., 8, 975–1003, https://doi.org/10.5194/gmd-8-975-2015, 2015.

Fu, D., Kulawik, S. S., Miyazaki, K., Bowman, K. W., Worden, J. R., Eldering, A., Livesey, N. J., Teixeira, J., Irion, F. W., Herman, R. L., Osterman, G. B., Liu, X., Levelt, P. F., Thompson, A. M. and Luo, M.: Retrievals of tropospheric ozone profiles from the synergism of AIRS and OMI: Methodology and validation, Atmos. Meas. Tech., 11, 5587–5605, https://doi.org/10.5194/amt-11-5587-2018, 2018.

Gaudel, A., Bourgeois, I., Li, M., Chang, K.-L., Ziemke, J., Sauvage, B., Stauffer, R. M., Thompson, A. M., Kollonige, D. E., Smith, N., Hubert, D., Keppens, A., Cuesta, J., Heue, K.-P., Veefkind, P., Aikin, K., Peischl, J., Thompson, C. R., Ryerson, T. B., Frost, G. J., McDonald, B. C., and Cooper, O. R.: Tropical tropospheric ozone distribution and trends from in situ and satellite data, Atmos. Chem. Phys., 24, 9975–10000, https://doi.org/10.5194/acp-24-9975-2024, 2024.

Gelaro, R., McCarty, W., Suárez, M. J., Todling, R., Molod, A., Takacs, L., Randles, C. A., Darmenov, A., Bosilovich, M. G., Reichle, R., Wargan, K., Coy, L., Cullather, R., Draper, C., Akella, S., Buchard, V., Conaty, A., da Silva, A. M., Gu, W., Kim, G.-K., Koster, R., Lucchesi, R., Merkova, D., Nielsen, J. E., Partyka, G., Pawson, S., Putman, W., Rienecker, M., Schubert, S. D., Sienkiewicz, M. and Zhao, B.: The Modern-Era Retrospective Analysis for Research and Applications, Version 2 (MERRA-2), J. Clim., 30, 5419–5454, https://doi.org/10.1175/JCLI-D-16-0758.1, 2017.

Gettelman, A., de F. Forster, P. M., Fujiwara, M., Fu, Q., Vömel, H., Gohar, L. K., Johanson, C., and Ammerman, M.: Radiation balance of the tropical tropopause layer, J. Geophys. Res., 109, D07103, https://doi.org/10.1029/2003JD004190, 2004.

Giglio, L., Schroeder, W. and Justice, C. O.: The collection 6 MODIS active fire detection algorithm and fire products, Remote Sens. Environ., 178, 31–41, https://doi.org/10.1016/j.rse.2016.02.054, 2016.

Granier, C., Bessagnet, B., Bond, T., D'Angiola, A., van der Gon, H. D., Frost, G. J., Heil, A., Kaiser, J. W., Kinne, S., Klimont, Z., Kloster, S., Lamarque, J.-F., Liousse, C., Masui, T., Meleux, F., Mieville, A., Ohara, T., Raut, J.-C., Riahi, K., Schultz, M. G., Smith, S. J., Thompson, A., van Aardenne, J., van der Werf, G. R. and van Vuuren, D. P.: Evolution of anthropogenic and biomass burning emissions of air pollutants at global and regional scales during the 1980–2010 period, Clim. Change, 109, 163–190, https://doi.org/10.1007/s10584-011-0154-1, 2011.

Granier, C., Lamarque,J. F., Mieville, A., Muller, J. F., Olivier, J., Orlando, J., Peters, J., Petron, G., Tyndall, G. and Wallens, S.: POET, a database of surface emissions of ozone precursors GEIA-ACCENT documentation http://www.pole-ether.fr/eccad, 2005

Guenther, A., Karl, T., Harley, P., Wiedinmyer, C., Palmer, P. I., and Geron, C.: Estimates of global terrestrial isoprene emissions using MEGAN (Model of Emissions of Gases and Aerosols from Nature), Atmos. Chem. Phys., 6, 3181–3210, https://doi.org/10.5194/acp-6-3181-2006, 2006.

Hersbach, H., Bell, B., Berrisford, P., Hirahara, S., Horányi, A., Muñoz-Sabater, J., Nicolas, J., Peubey, C., Radu, R., Schepers, D., Simmons, A., Soci, C., Abdalla, S., Abellan, X., Balsamo, G., Bechtold, P., Biavati, G., Bidlot, J., Bonavita, M., De Chiara, G., Dahlgren, P., Dee, D., Diamantakis, M., Dragani, R., Flemming, J., Forbes, R., Fuentes, M., Geer, A., Haimberger, L., Healy, S., Hogan, R. J., Hólm, E., Janisková, M., Keeley, S., Laloyaux, P., Lopez, P., Lupu, C., Radnoti, G., de Rosnay, P., Rozum, I., Vamborg, F., Villaume, S. and Thépaut, J. N.: The ERA5 global reanalysis, Q. J. R. Meteorol. Soc., 146, 1999–2049, https://doi.org/10.1002/qj.3803, 2020.

Huijnen, V., Miyazaki, K., Flemming, J., Inness, A., Sekiya, T. and G. Schultz, M.: An intercomparison of tropospheric ozone reanalysis products from CAMS, CAMS interim, TCR-1, and TCR-2, Geosci. Model Dev., 13, 1513–1544, https://doi.org/10.5194/gmd-13-1513-2020, 2020.

Hurtmans, D., Coheur, P.-F., Wespes, C., Clarisse, L., Scharf, O., Clerbaux, C., Hadji-Lazaro, J., George, M. and Turquety, S.: FORLI radiative transfer and retrieval code for IASI, J. Quant. Spectrosc. Radiat. Transf., 113, 1391–1408, https://doi.org/10.1016/j.jqsrt.2012.02.036, 2012.

Inness, A., Ades, M., Agustí-Panareda, A., Barré, J., Benedictow, A., Blechschmidt, A.-M., Dominguez, J. J., Engelen, R., Eskes, H., Flemming, J., Huijnen, V., Jones, L., Kipling, Z., Massart, S., Parrington, M., Peuch, V.-H., Razinger, M., Remy, S., Schulz, M. and Suttie, M.: The CAMS reanalysis of atmospheric composition, Atmos. Chem. Phys., 19, 3515–3556, https://doi.org/10.5194/acp-2018-1078, 2019.

Janssens-Maenhout, G., Crippa, M., Guizzardi, D., Dentener, F., Muntean, M., Pouliot, G., Keating, T., Zhang, Q., Kurokawa, J., Wankmüller, R., Denier van der Gon, H., Kuenen, J. J. P., Klimont, Z., Frost, G., Darras, S., Koffi, B. and Li, M.:

HTAP_v2.2: a mosaic of regional and global emission grid maps for 2008 and 2010 to study hemispheric transport of air pollution, Atmos. Chem. Phys., 15, 11411–11432, https://doi.org/10.5194/acp-15-11411-2015, 2015.

Kaiser, J. W., Heil, A., Andreae, M. O., Benedetti, A., Chubarova, N., Jones, L., Morcrette, J.-J., Razinger, M., Schultz, M. G., Suttie, M. and van Der Werf, G. R.: Biomass burning emissions estimated with a global fire assimilation system based on observed fire radiative power, Biogeosciences, 9, 527–554, https://doi.org/10.5194/bg-9-527-2012, 2012.

Kaplan, J. O. and Lau, K. H.-K.: The WGLC global gridded lightning climatology and time series, Earth Syst. Sci. Data, 13, 3219–3237, https://doi.org/10.5194/essd-13-3219-2021, 2021a.

Kaplan, J. O. and Lau, K. H.-K.: The WWLLN Global Lightning Climatology and timeseries (WGLC) (v2022.0.0), Zenodo [data set], https://doi.org/10.5281/zenodo.6007052, 2021b.

Kondo, Y., Morino, Y., Takegawa, N., Koike, M., Kita, K., Miyazaki, Y., Sachse, G. W., Vay, S. A., Avery, M. A., Flocke, F., Weinheimer, A. J., Eisele, F. L., Zondlo, M. A., Weber, R. J., Singh, H. B., Chen, G., Crawford, J., Blake, D. R., Fuelberg, H. E., Clarke, A. D., Talbot, R. W., Sandholm, S. T., Browell, E. V., Streets, D. G. and Liley, B.: Impacts of biomass burning in Southeast Asia on ozone and reactive nitrogen over the western Pacific in spring, J. Geophys. Res.-Atmos., 109, D15S12, https://doi.org/10.1029/2003JD004203, 2004.

Krishnamurti, T. N., Sinha, M. C., Kanamitsu, M., Oosterhof, D., Fuelberg, H., Chatfield, R., Jacob, D. J. and Logan, J.: Passive tracer transport relevant to the TRACE A experiment, J. Geophys. Res., 101, 23889–23907, https://doi.org/10.1029/95JD02419, 1996.

Lacima, A., Petetin, H., Soret, A., Bowdalo, D., Jorba, O., Chen, Z., Méndez Turrubiates, R. F., Achebak, H., Ballester, J. and García-Pando, C. P.: Long-term evaluation of surface air pollution in CAMSRA and MERRA-2 global reanalyses over Europe (2003–2020), Geosci. Model Dev., 16, 2689–2718, https://doi.org/10.5194/gmd-16-2689-2023, 2023.

Lannuque, V., Sauvage, B., Barret, B., Clark, H., Athier, G., Boulanger, D., Cammas, J.-P., Cousin, J.-M., Fontaine, A., Le Flochmoën, E., Nédélec, P., Petetin, H., Pfaffenzeller, I., Rohs, S., Smit, H. G. J., Wolff, P. and Thouret, V.: Origins and characterization of CO and O_3 in the African upper troposphere, Atmos. Chem. Phys., 21, 14535–14555, https://doi.org/10.5194/acp-21-14535-2021, 2021.

Liebmann, B., and Smith, C. A.: Description of a Complete (Interpolated) Outgoing Longwave Radiation Dataset. Bull. Amer. Meteor. Soc., 77, 1275–1277. http://www.jstor.org/stable/26233278, 1996.

Liu, X., Bhartia, P. K., Chance, K., Spurr, R. J. D. and Kurosu, T. P.: Ozone profile retrievals from the Ozone Monitoring Instrument, Atmos. Chem. Phys., 10, 2521–2537, https://doi.org/10.5194/acp-10-2521-2010, 2010.

Lahoz, W. A. and Schneider, P.: Data assimilation: making sense of Earth Observation, Front. Environ. Sci., 2, https://doi.org/10.3389/fenvs.2014.00016, 2014.

Meijer, E. W., van Velthoven, P. F. J., Brunner, D. W., Huntrieser, H. and Kelder, H.: Improvement and evaluation of the parameterisation of nitrogen oxide production by lightning, Phys. Chem. Earth (C), 26, 577-583, https://doi.org/10.1016/S1464-1917(01)00050-2, 2001.

Miyazaki, K., Bowman, K., Sekiya, T., Eskes, H., Boersma, F., Worden, H., Livesey, N., Payne, V. H., Sudo, K., Kanaya, Y., Takigawa, M., and Ogochi, K.: Chemical Reanalysis Products, Jet Propulsion Laboratory [data set], https://doi.org/10.25966/9qgv-fe81, 2019.

Miyazaki, K., Bowman, K., Sekiya, T., Eskes, H., Boersma, F., Worden, H., Livesey, N., Payne, V. H., Sudo, K., Kanaya, Y., Takigawa, M. and Ogochi, K.: Updated tropospheric chemistry reanalysis and emission estimates, TCR-2, for 2005-2018, Earth Syst. Sci. Data, 12, 2223–2259, https://doi.org/10.5194/essd-12-2223-2020, 2020.

Miyazaki, K., Eskes, H. J. and Sudo, K.: A tropospheric chemistry reanalysis for the years 2005–2012 based on an assimilation of OMI, MLS, TES, and MOPITT satellite data, Atmos. Chem. Phys., 15, 8315–8348, https://doi.org/10.5194/acp-15-8315-2015, 2015.

Miyazaki, K., Eskes, H., Sudo, K., Boersma, K. F., Bowman, K., and Kanaya, Y.: Decadal changes in global surface NO_X emissions from multi-constituent satellite data assimilation, Atmos. Chem. Phys., 17, 807–837, https://doi.org/10.5194/acp-17-807-2017, 2017.

Monks, P. S., Archibald, A. T., Colette, A., Cooper, O., Coyle, M., Derwent, R., Fowler, D., Granier, C., Law, K. S., Mills, G. E., Stevenson, D. S., Tarasova, O., Thouret, V., von Schneidemesser, E., Sommariva, R., Wild, O. and Williams, M. L.: Tropospheric ozone and its precursors from the urban to the global scale from air quality to short-lived climate forcer, Atmos. Chem. Phys., 15, 8889–8973, https://doi.org/10.5194/acp-15-8889-2015, 2015.

Moxim, W. J. and Levy II, H.: A model analysis of the tropical South Atlantic Ocean tropospheric ozone maximum: The interaction of transport and chemistry, J. Geophys. Res., 105, 17393–17415, https://doi.org/10.1029/2000JD900175, 2000.

Nussbaumer, C. M., Fischer, H., Lelieveld, J., and Pozzer, A.: What controls ozone sensitivity in the upper tropical troposphere?, Atmos. Chem. Phys., 23, 12651–12669, https://doi.org/10.5194/acp-23-12651-2023, 2023.

Okamoto, S., Cuesta, J., Beekmann, M., Dufour, G., Eremenko, M., Miyazaki, K., Boonne, C., Tanimoto, H. and Akimoto, H.: Impact of different sources of precursors on an ozone pollution outbreak over Europe analysed with IASI+GOME2 multispectral satellite observations and model simulations, Atmos. Chem. Phys., 23, 7399–7423, https://doi.org/10.5194/acp-23-7399-2023, 2023.

Olivier J., Peters, J., Granier, C., Petron, G., Muller J. F. and Wallens, S.: Present and future surface emissions of atmospheric compounds GEIA-ACCENT documentation POET report #2, EU project EVK2-1999-00011, 2003

Ott, L. E., Pickering, K. E., Stenchikov, G. L., Allen, D. J., DeCaria, A. J., Ridley, B., Lin, R.-F., Lang, S. and Tao, W.-K.: Production of lightning NOx and its vertical distribution calculated from three-dimensional cloud-scale chemical transport model simulations, J. Geophys. Res., 115, D04301, https://doi.org/10.1029/2009JD011880, 2010.

Park, M., Randel, W. J., Gettelman, A., Massie, S. T., and Jiang, J. H.: Transport above the Asian summer monsoon anticyclone inferred from Aura Microwave Limb Sounder tracers, J. Geophys. Res., 112, D16309, https://doi.org/10.1029/2006JD008294, 2007.

Park, S., Son, S. W., Jung, M. Il, Park, J. and Park, S. S.: Evaluation of tropospheric ozone reanalyses with independent ozonesonde observations in East Asia, Geosci. Lett., 7, https://doi.org/10.1186/s40562-020-00161-9, 2020.

Pereira, G., Longo, K. M., Freitas, S. R., Mataveli, G., Oliveira, V. J., Santos, P. R., Rodrigues, L. F. and Cardozo, F. S.: Improving the south America wildfires smoke estimates: Integration of polar-orbiting and geostationary satellite fire products in the Brazilian biomass burning emission model (3BEM), Atmos. Environ., 273, 118954, https://doi.org/10.1016/j.atmosenv.2022.118954, 2022.

Peterson, M.: FORTE Measurements of Global Lightning Altitudes, Earth Sp. Sci., 9, 1–22, https://doi.org/10.1029/2022EA002404, 2022.

Petzold, A., Thouret, V., Gerbig, C., Zahn, A., Brenninkmeijer, C. A. M., Gallagher, M., Hermann, M., Pontaud, M., Ziereis, H., Boulanger, D., Marshall, J., Nédélec, P., Smit, H. G. J., Friess, U., Flaud, J.-M., Wahner, A., Cammas, J.-P., Volz-Thomas, A., and IAGOS TEAM: Global-scale atmosphere monitoring by in-service aircraft – current achievements and future prospects of the European Research Infrastructure IAGOS, Tellus B, 6, 1–24, https://doi.org/10.3402/tellusb.v67.28452, 2015.

Pickering, K. E., Thompson, A. M., Wang, Y., Tao, W.-K., McNamara, D. P., Kirchhoff, V. W. J. H., Heikes, B. G., Sachse, G. W., Bradshaw, J. D., Gregory, G. L. and Blake, D. R.: Convective transport of biomass burning emissions over Brazil during TRACE A, J. Geophys. Res., 101, 23993–24012, https://doi.org/10.1029/96JD00346, 1996.

Price, C. and Rind, D.: A simple lightning parameterization for calculating global lightning distributions, J. Geophys. Res., 97, 9919–9933, https://doi.org/10.1029/92JD00719, 1992.

Randerson, J. T., van der Werf, G. R., Giglio, L., Collatz, G. J., and Kasibhatla, P.S.: Global Fire Emissions Database, Version 4.1 (GFEDv4) [data set], https://doi.org/10.3334/ORNLDAAC/1293, 2018.

Ray, E. A.: ATom: Back Trajectories and Influences of Air Parcels Along Flight Track, 2016-2018 [data set], https://doi.org/10.3334/ORNLDAAC/1889, 2021.

Roberts, G., Wooster, M. J. and Lagoudakis, E.: Annual and diurnal african biomass burning temporal dynamics, Biogeosciences, 6, 849–866, https://doi:10.5194/bg-6-849-2009, 2009.

Ryu, Y.-H. and Min, S.-K.: Long-term evaluation of atmospheric composition reanalyses from CAMS, TCR-2, and MERRA-2 over South Korea: Insights into applications, implications, and limitations, Atmos. Environ., 246, 118062, https://doi.org/10.1016/j.atmosenv.2020.118062, 2021.

Sauvage, B., Martin, R. V., van Donkelaar, A. and Ziemke, J. R.: Quantification of the factors controlling tropical tropospheric ozone and the South Atlantic maximum, J. Geophys. Res. Atmos., 112, D11309, https://doi.org/10.1029/2006JD008008, 2007a.

Sauvage, B., Thouret, V., Cammas, J.-P., Brioude, J., Nédélec, P., and Mari C.: Meridional ozone gradients in the African upper troposphere, Geophys. Res. Lett., 34, L03817, https://doi:10.1029/2006GL028542, 2007b.

Sauvage, B., Thouret, V., Cammas, J.-P., Gheusi, F., Athier, G., and Nédélec, P.: Tropospheric ozone over Equatorial Africa: regional aspects from the MOZAIC data, Atmos. Chem. Phys., 5, 311–335, https://doi.org/10.5194/acp-5-311-2005, 2005.

Schumann, U. and Huntrieser, H.: The global lightning-induced nitrogen oxides source, Atmos. Chem. Phys., 7, 3823–3907, https://doi.org/10.5194/acp-7-3823-2007, 2007.

Sindelarova, K., Granier, C., Bouarar, I., Guenther, A., Tilmes, S., Stavrakou, T., Müller, J.-F., Kuhn, U., Stefani, P., and Knorr, W.: Global data set of biogenic VOC emissions calculated by the MEGAN model over the last 30 years, Atmos. Chem. Phys., 14, 9317–9341, https://doi.org/10.5194/acp-14-9317-2014, 2014.

Sindelarova, K., Markova, J., Simpson, D., Huszar, P., Karlicky, J., Darras, S. and Granier, C.: High-resolution biogenic global emission inventory for the time period 2000–2019 for air quality modelling, Earth Syst. Sci. Data, 14, 251–270, https://doi.org/10.5194/essd-14-251-2022, 2022.

Škerlak, B., Sprenger, M., and Wernli, H.: A global climatology of stratosphere-troposphere exchange using the ERA-Interim data set from 1979 to 2011. Atmos. Chem. Phys., 14, 913–937. https://doi.org/10.5194/acp-14-913-2014, 2014.

Spurr, R. J. D.: VLIDORT: A linearized pseudo-spherical vector discrete ordinate radiative transfer code for forward model and retrieval studies in multilayer multiple scattering media, J. Quant. Spectrosc. Radiat. Transf., 102, 316–342, https://doi.org/10.1016/j.jqsrt.2006.05.005, 2006.

Stein, O., Schultz, M. G., Bouarar, I., Clark, H., Huijnen, V., Gaudel, A., George, M. and Clerbaux, C.: On the wintertime low bias of Northern Hemisphere carbon monoxide found in global model simulations, Atmos. Chem. Phys., 14, 9295–9316, https://doi.org/10.5194/acp-14-9295-2014, 2014.

Stiller, G. P., von Clarmann, T., Funke, B., Glatthor, N., Hase, F., Höpfner, M. and Linden, A.: Sensitivity of trace gas abundances retrievals from infrared limb emission spectra to simplifying approximations in radiative transfer modelling, J. Quant. Spectrosc. Radiat. Transf., 72, 249–280, https://doi.org/10.1016/S0022-4073(01)00123-6, 2002.

Stroppiana, D., Brivio, P. A., Grégoire, J.-M., Liousse, C., Guillaume, B., Granier, C., Mieville, A., Chin, M., and Pétron, G.: Comparison of global inventories of CO emissions from biomass burning derived from remotely sensed data, Atmos. Chem. Phys., 10, 12173–12189, https://doi.org/10.5194/acp-10-12173-2010, 2010.

Szopa, S., Naik, V., Adhikary, B., Artaxo, P., Berntsen, T., Collins, W. D., Fuzzi, S., Gallardo, L., Kiendler-Scharr, A., Klimont, Z., Liao, H., Unger, N., and Zanis, P.: Short-Lived Climate Forcers, in: Climate Change 2021: The Physical Science Basis. Contribution of Working Group I to the Sixth Assessment Report of the Intergovernmental Panel on Climate Change, edited by: Masson-Delmotte, V., Zhai, P., Pirani, A., Connors, S. L., Péan, C., Berger, S., Caud, N., Chen, Y., Goldfarb, L., Gomis, M. I., Huang, M., Leitzell, K., Lonnoy, E., Matthews, J. B. R., Maycock, T. K., Waterfield, T., Yelekçi, O., Yu, R., and Zhou, B., Cambridge University Press, Cambridge, United Kingdom and New York, NY, USA, 817–922, https://doi.org/10.1017/9781009157896.008, 2021.

Thompson, A. M., Doddridge, B. G., Witte, J. C., Hudson, R. D., Luke, W. T., Johnson, J. E., Johnson, B. J., Oltmans, S. J., Weller, R.: A tropical Atlantic Paradox: Shipboard and satellite views of a tropospheric ozone maximum and wave-one in January–February 1999, Geophys. Res. Lett., https://doi.org/10.1029/1999GL011273, 2000.

Thompson, A. M., Pickering, K. E., McNamara, D. P., Schoeberl, M. R., Hudson, R. D., Kim, J. H., Browell, E. V., Kirchhoff, V. W. J. H. and Nganga, D.: Where did tropospheric ozone over southern Africa and the tropical Atlantic come from in October 1992? Insights from TOMS, GTE TRACE A, and SAFARI 1992, J. Geophys. Res., 101, 24251–24278, https://doi.org/10.1029/96JD01463, 1996.

Thompson, A. M., Stauffer, R. M., Wargan, K., Witte, J. C., Kollonige, D. E. and Ziemke, J. R.: Regional and seasonal trends in tropical ozone from SHADOZ profiles: Reference for models and satellite products. J. Geophys. Res. Atmos., 126, e2021JD034691, https://doi.org/10.1029/2021JD034691, 2021.

Thompson, A. M., Witte, J. C., Oltmans, S. J., Schmidlin, F. J., Logan, J. A., Fujiwara, M., Kirchhoff, V. W. J. H., Posny, F., Coetzee, G. J. R., Hoegger, B., Kawakami, S., Ogawa, T., Fortuin, J. P. F. and Kelder, H. M.: Southern Hemisphere Additional Ozonesondes (SHADOZ) 1998–2000 tropical ozone climatology 2. Tropospheric variability and the zonal wave-one, J. Geophys. Res., 108, 8241, https://doi.org/10.1029/2002JD002241, 2003.

Thompson, A. M., Witte, J. C., Sterling, C., Jordan, A., Johnson, B. J., Oltmans, S. J., Fujiwara, M., Vömel, H., Allaart, M., Piters, A., Coetzee, G. J. R., Posny, F., Corrales, E., Andres Diaz, J., Félix, C., Komala, N., Lai, N., Ahn Nguyen, H. T., Maata, M., Mani, F., Zainal, Z., Ogino, S., Paredes, F., Penha, T. L. B., Raimundo da Silva, F., Sallons-Mitro, S., Selkirk, H. B., Schmidlin, F. J., Stübi, R. and Thiongo, K.: First reprocessing of Southern Hemisphere Additional Ozonesondes (SHADOZ) ozone profiles (1998–2016): 2. Comparisons with satellites and ground-based instruments. J. Geophys. Res. Atmos., 122, 13000–13025, https://doi.org/10.1002/2017JD027406, 2017.

Thompson, C. R., Wofsy, S. C., Prather, M. J., Newman, P. A., Hanisco, T. F., Ryerson, T. B., Fahey, D. W., Apel, E. C., Brock, C. A., Brune, W. H., Froyd, K., Katich, J. M., Nicely, J. M., Peischl, J., Ray, E., Veres, P. R., Wang, S., Allen, H. M., Asher, E., Bian, H., Blake, D., Bourgeois, I., Budney, J., Bui, T. P., Butler, A., Campuzano-Jost, P., Chang, C., Chin, M., Commane, R., Correa, G., Crounse, J. D., Daube, B., Dibb, J. E., DiGangi, J. P., Diskin, G. S., Dollner, M., Elkins, J. W., Fiore, A. M., Flynn, C. M., Guo, H., Hall, S. R., Hannun, R. A., Hills, A., Hintsa, E. J., Hodzic, A., Hornbrook, R. S., Huey, L. G., Jimenez, J. L., Keeling, R. F., Kim, M. J., Kupc, A., Lacey, F., Lait, L. R., Lamarque, J.-F., Liu, J., McKain, K., Meinardi, S., Miller, D. O., Montzka, S. A., Moore, F. L., Morgan, E. J., Murphy, D. M., Murray, L. T., Nault, B. A., Neuman, J. A., Nguyen, L., Gonzalez, Y., Rollins, A., Rosenlof, K., Sargent, M., Schill, G., Schwarz, J. P., Clair, J. M. S., Steenrod, S. D., Stephens, B. B., Strahan, S. E., Strode, S. A., Sweeney, C., Thames, A. B., Ullmann, K., Wagner, N., Weber, R., Weinzierl, B., Wennberg, P. O., Williamson, C. J., Wolfe, G. M., and Zeng, L.: The NASA Atmospheric Tomography (ATom) Mission: Imaging the Chemistry of the Global Atmosphere, Bull. Amer. Meteor. Soc., 103, E761–E790, https://doi.org/10.1175/BAMS-D-20-0315.1, 2022.

Tsivlidou, M., Sauvage, B., Bennouna, Y., Blot, R., Boulanger, D., Clark, H., Le Flochmoën, E., Nédélec, P., Thouret, V., Wolff, P., and Barret, B.: Tropical tropospheric ozone and carbon monoxide distributions: characteristics, origins, and control factors, as seen by IAGOS and IASI, Atmos. Chem. Phys., 23, 14039–14063, https://doi.org/10.5194/acp-23-14039-2023, 2023.

van der Werf, G. R., Randerson, J. T., Giglio, L., Collatz, G. J., Kasibhatla, P. S., and Arellano Jr., A. F.: Interannual variability in global biomass burning emissions from 1997 to 2004, Atmos. Chem. Phys., 6, 3423–3441, https://doi.org/10.5194/acp-6-3423-2006, 2006.

van der Werf, G. R., Randerson, J. T., Giglio, L., van Leeuwen, T. T., Chen, Y., Rogers, B. M., Mu, M., van Marle, M. J. E., Morton, D. C., Collatz, G. J., Yokelson, R. J. and Kasibhatla, P. S.: Global fire emissions estimates during 1997–2016, Earth Syst. Sci. Data, 9, 697–720, https://doi.org/10.5194/essd-9-697-2017, 2017.

Watanabe, S., Hajima, T., Sudo, K., Nagashima, T., Takemura, T., Okajima, H., Nozawa, T., Kawase, H., Abe, M., Yokohata, T., Ise, T., Sato, H., Kato, E., Takata, K., Emori, S. and Kawamiya, M.: MIROC-ESM 2010: model description and basic results of CMIP5-20c3m experiments, Geosci. Model Dev., 4, 845–872, https://doi.org/10.5194/gmd-4-845-2011, 2011.

Weller, R., Lilischkis, R., Schrems, O., Neuber, R. and Wessel, S.: Vertical ozone distribution in the marine atmosphere over the central Atlantic Ocean (56°S – 50°N), J. Geophys. Res., 101, 1387–1399, https://doi.org/10.1029/95JD02838, 1996.

Williams, R. S., Hegglin, M. I., Kerridge, B. J., Jöckel, P., Latter, B. G., and Plummer, D. A.: Characterising the seasonal and geographical variability in tropospheric ozone, stratospheric influence and recent changes, Atmos. Chem. Phys., 19, 3589–3620, https://doi.org/10.5194/acp-19-3589-2019, 2019.

Wofsy, S. C., Afshar, S., Allen, H. M., Apel, E. C., Asher, E. C., Barletta, B., Bent, J., Bian, H., Biggs, B. C., Blake, D. R., Blake, N., Bourgeois, I., Brock, C. A., Brune, W. H., Budney, J. W., Bui, T. P., Butler, A., Campuzano-Jost, P., Chang, C. S., Chin, M., Commane, R., Correa, G., Crounse, J. D., Cullis, P. D., Daube, B. C., Day, D. A., Dean-Day, J. M., Dibb, J. E., DiGangi, J. P., Diskin, G. S., Dollner, M., Elkins, J. W., Erdesz, F., Fiore, A. M., Flynn, C. M., Froyd, K. D., Gesler, D. W., Hall, S. R., Hanisco, T. F., Hannun, R. A., Hills, A. J., Hintsa, E. J., Hoffman, A., Hornbrook, R. S., Huey, L. G., Hughes, S., Jimenez, J. L., Johnson, B. J., Katich, J. M., Keeling, R. F., Kim, M. J., Kupc, A., Lait, L. R., Lamarque, J.-F., Liu, J., McKain, K., Mclaughlin, R. J., Meinardi, S., Miller, D. O., Montzka, S. A., Moore, F. L., Morgan, E. J., Murphy, D. M., Murray, L. T., Nault, B. A., Neuman, J. A., Newman, P. A., Nicely, J. M., Pan, X., Paplawsky, W., Peischl, J., Prather, M. J., Price, D. J., Ray, E. A., Reeves, J. M., Richardson, M., Rollins, A. W., Rosenlof, K. H., Ryerson, T. B., Scheuer, E., Schill, G. P., Schroder, J. C., Schwarz, J. P., St.Clair, J. M., Steenrod, S. D., Stephens, B. B., Strode, S. A., Sweeney, C., Tanner, D., Teng, A. P., Thames, A. B., Thompson, C. R., Ullmann, K., Veres, P. R., Vieznor, N., Wagner, N. L., Watt, A., Weber, R., Weinzierl, B. B., Wennberg, P. O., Williamson, C. J., Wilson, J. C., Wolfe, G. M., Woods, C. T., and Zeng, L. H.: ATom: Merged Atmospheric Chemistry, Trace Gases, and Aerosols [data set], https://doi.org/10.3334/ORNLDAAC/1581, 2018.

Yamasoe, M. A., Sauvage, B., Thouret, V., Nédélec, P., Le Flochmoen, E., and Barret, B.: Analysis of tropospheric ozone and carbon monoxide profiles over South America based on MOZAIC/IAGOS database and model simulations, Tellus B, 67, 27884, https://doi.org/10.3402/tellusb.v67.27884, 2015.

Yang, H., Chen, G., Tang, Q., and Hess, P.: Quantifying isentropic stratosphere-troposphere exchange of ozone, J. Geophys. Res. Atmos., 121, 3372–3387, https://doi.org/10.1002/2015jd024180, 2016.Yienger, J. J. and Levy II, H.: Empirical model of global soil-biogenic NOX emissions, J. Geophys. Res., 100, 11447–11464, https://doi.org/10.1029/95JD00370, 1995.

Young, P. J., Archibald, A. T., Bowman, K. W., Lamarque, J.-F., Naik, V., Stevenson, D. S., Tilmes, S., Voulgarakis, A., Wild, O., Bergmann, D., Cameron-Smith, P., Cionni, I., Collins, W. J., Dalsøren, S. B., Doherty, R. M., Eyring, V., Faluvegi, G., Horowitz, L. W., Josse, B., Lee, Y. H., MacKenzie, I. A., Nagashima, T., Plummer, D. A., Righi, M., Rumbold, S. T.,

Skeie, R. B., Shindell, D. T., Strode, S. A., Sudo, K., Szopa, S. and Zeng, G.: Pre-industrial to end 21st century projections of tropospheric ozone from the Atmospheric Chemistry and Climate Model Intercomparison Project (ACCMIP), Atmos. Chem. Phys., 13, 2063–2090, https://doi.org/10.5194/acp-13-2063-2013, 2013.

Zhang, Y., Li, J., Li, J., Pan, X., Wang, W., Zhu, L., Wang, Z., Chen, X., Yang, W. and Wang, Z.: An intercomparison of ozone taken from the Copernicus atmosphere monitoring service and the second Modern-Era retrospective analysis for research and applications over China during 2018 and 2019, J. Environ. Sci., 114, 514–525, https://doi.org/10.1016/j.jes.2022.01.045, 2022.

Zheng, B., Chevallier, F., Ciais, P., Yin, Y. and Wang, Y.: On the role of the flaming to smoldering transition in the seasonal cycle of African fire emissions. Geophys. Res. Lett., 45, 11998–12007, https://doi.org/10.1029/2018GL079092, 2018.